CHEMISTRY OF MATERIALS

pubs.acs.org/cm Article

Understanding How Ligand Functionalization Influences CO_2 and N_2 Adsorption in a Sodalite Metal–Organic Framework

Mehrdad Asgari, Rocio Semino, Pascal A. Schouwink, Ilia Kochetygov, Jacob Tarver, Olga Trukhina, Rajamani Krishna, Craig M. Brown, Michele Ceriotti, and Wendy L. Queen*

Cite This: *Chem. Mater.* 2020, 32, 1526–1536 Read Online

ACCESS | Metrics & More | Article Recommendations | Supporting Information

ABSTRACT: In this work, a detailed study is conducted to understand how ligand substitution influences the CO_2 and N_2 adsorption properties of two highly crystalline sodalite metal–organic frameworks (MOFs) known as Cu–BTT (BTT^{-3} = 1,3,5-benzenetristetrazolate) and Cu–BTTri ($BTTri^{-3}$ = 1,3,5-benzenetristriazolate). The enthalpy of adsorption and observed adsorption capacities at a given pressure are significantly lower for Cu–BTTri compared to its tetrazole counterpart, Cu–BTT. In situ X-ray and neutron diffraction, which allow visualization of the CO_2 and N_2 binding sites on the internal surface of Cu–BTTri, provide insights into understanding the subtle differences. As expected, slightly elongated distances between the open Cu^{2+} sites and surface-bound CO_2 in Cu–BTTri can be explained by the fact that the triazolate ligand is a better electron donor than the tetrazolate. The more pronounced Jahn–Teller effect in Cu–BTTri leads to weaker guest binding. The results of the aforementioned structural analysis were complemented by the prediction of the binding energies at each CO_2 and N_2 adsorption site by density functional theory calculations. In addition, variable temperature in situ diffraction measurements shed light on the fine structural changes of the framework and CO_2 occupancies at different adsorption sites as a function of temperature. Finally, simulated breakthrough curves obtained for both sodalite MOFs demonstrate the materials' potential performance in dry postcombustion CO_2 capture. The simulation, which considers both framework uptake capacity and selectivity, predicts better separation performance for Cu–BTT. The information obtained in this work highlights how ligand substitution can influence adsorption properties and hence provides further insights into the material optimization for important separations.

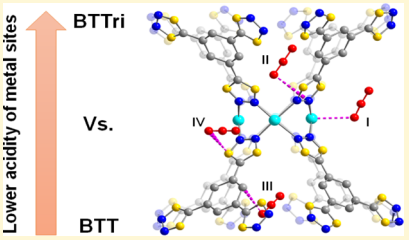

INTRODUCTION

Since the industrial revolution, the combustion of carbon-based fuels has led to a significant rise in atmospheric CO_2 levels, one of the main causes of global warming.[1] During the last few years, the concentration of atmospheric CO_2 has surpassed a record value of 400 ppm.[2] This, combined with a slow transition to clean, renewable energy sources, has brought a sense of urgency toward the design of new porous solid adsorbents[3−6] able to capture CO_2 from a variety of gas mixtures, such as postcombustion flue gas.[7]

One possible solution to this problem is a class of porous crystalline materials, known as metal–organic frameworks (MOFs), which consist of metal-ions or metal-ion clusters that are interlinked by organic ligands. These unique materials offer unprecedented internal surface area and easy chemical tunability, allowing chemists to readily adjust their adsorption properties.[4,8−10] The presence of metal ions and multiple types of chemical moieties on the organic building blocks create a potential energy landscape with multiple minima for an incoming guest species; this corresponds to well-defined adsorption sites with varying binding energies.[11] Considering this, these materials offer a unique opportunity to gain direct insight into their structure-derived function using X-ray and neutron diffraction techniques. Diffraction data provide binding mechanisms, reveal the relative differences in binding energies between neighboring adsorption sites, and deliver understanding of how the local framework structure changes as a function of external stimuli, such as temperature or pressure. Such insight makes it possible to pinpoint the structural features that give rise to enhanced or diminished adsorption properties. Further, diffraction data can be employed to validate computational methods meant to predict the structure and adsorption properties of MOFs.[6] This validation process is necessary for the eventual deployment of simulation tools that can accurately predict the properties of hypothetical MOF structures, a process that might allow for the rapid identification of target materials having optimal properties for important gas separations, such as CO_2 capture.

MOFs bearing azole-containing ligands are becoming increasingly prevalent in the literature.[12,13] Their popularity stems from strong metal–nitrogen bonds, a phenomenon that often leads to higher chemical and thermal stability when

Received: November 8, 2019
Revised: January 29, 2020
Published: January 29, 2020

https://dx.doi.org/10.1021/acs.chemmater.9b04631
Chem. Mater. 2020, 32, 1526–1536

compared to their carboxylate counterparts.[14,15] One prevalent example of a family of azole frameworks is M−BTT (M = Mg, Ca, Ti, V, Cr, Mn, Fe, Co, Ni, Cu, and Zn; BTT^{3-} = 1,3,5-benzenetristetrazolate), which has the following general formula: $[(M_4Cl_x)_3(BTT)_8]^{y-}$ (x = 0 or 1; y = 0 or −3).[16] The MOF features truncated, octahedral cages constructed by six $[M_4Cl_x]^{(8-x)+}$ units and eight $[BTT]^{3-}$ ligands that are interlinked to form a porous, three-dimensional sodalite-based network. In addition to high stability, this family of MOFs possesses a high density of open metal coordination sites (OMCs), which are capable of forming strong interactions with small molecules such as CO_2; thus, the adsorption properties of the framework are readily modified by altering the metal identity. Given this, in previous work, we employed in situ diffraction techniques, combined with density functional theory (DFT) to rationalize how metal-substitution influences the CO_2 adsorption properties of several isostructural M−BTT (M = Fe, Mn, Cu, Cr) frameworks.[16] In addition to varying metals, the tetrazole ligand can also be replaced with a triazole or pyrazole (BTT^{3-} vs $BTTri^{3-}$ = 1,3,5-benzenetristriazolate or BTP^{3-} = 1,3,5-benzenetrispyrazolate) forming similar sodalite architectures;[15−19] however, the resulting materials show dissimilar adsorption properties because of the distinct structural features that are induced by the ligand selection. Given that the aforementioned sodalite MOFs can undergo extensive chemical substitution and often exhibit exceptional crystallinity, they are of interest for in situ diffraction studies.[15] We have previously shown that the substitution of the BTT^{3-} ligand with $BTTri^{3-}$ causes a change in the structure of the metal cluster and the framework charge, and eliminates the existence of charge-balancing cations and anions in the channel of Cu−BTTri.[20] In the current work, we extend this study to unveil how ligand substitution influences the CO_2 and N_2 adsorption properties of Cu−BTTri compared to Cu−BTT. For this, both single-component N_2 and CO_2 adsorption isotherms and in situ diffraction techniques, coupled with DFT calculations are used. The diffraction results unveil the structures of the CO_2 and N_2 adsorbed Cu−BTTri framework, providing molecular level insight into how the presence of the triazole influences the CO_2 adsorption isotherms. The characterization of the structure and adsorption properties of the different sites are compared to DFT calculations used to predict the structure and binding energies of Cu−BTTri containing CO_2. Finally, transient breakthrough simulations are used to provide insight into the performance of the Cu−BTT and Cu−BTTri for CO_2/N_2 separation under dry, postcombustion flue gas conditions. This work links the structural parameters of two Cu-containing frameworks to the CO_2 and N_2 adsorption properties, which influence the materials' overall performance for postcombustion flue gas separations. The combined experimental and computational effort allows us to rationalize the structure−property relationships in these two sodalite MOFs, work that can hopefully help inform the design of MOFs optimized for such separations.

EXPERIMENTAL SECTION

Synthesis of Cu−BTTri. The H_3BTTri ligand was first synthesized following a procedure that was reported previously in the literature.[15] Subsequently, Cu−BTTri was synthesized, solvent exchanged and activated following a procedure reported previously by us.[20]

Standard Adsorption Isotherm Measurements. For gas adsorption isotherms, UHP-grade (99.999% purity) helium, nitrogen, and carbon dioxide were used for all measurements at pressures that ranged from 0 to 1 bar using a commercial BELSORP-max instrument. The sample was transferred to preweighed analysis tubes that were capped with a TRANSEAL. The sample was first evacuated on the activation station based on the program described in the literature.[15] The evacuated analysis tube containing the sample was then carefully transferred to an electronic balance and reweighed to determine the mass of the activated sample (typically ranging 50−200 mg). Then, the tube was transferred to the BELSORP-max. N_2 adsorption isotherms were collected at 77 K and Brunauer−Emmett−Teller (BET) surface areas and pore volumes were calculated assuming a value of 16.2 $Å^2$ for the molecular cross-sectional area of N_2. In addition, N_2 adsorption isotherms were measured at temperatures ranging from 278 K to 298 K. For CO_2, standard adsorption isotherms were measured using a commercial water bath dewar vessel connected to a Julabo F32-MC isothermal bath at temperatures ranging from 278 to 318 K.

In Situ Neutron Diffraction. High-resolution neutron powder diffraction (NPD) experiments were carried out on the Cu−BTTri sample using BT1 at the National Institute of Standards and Technology (NIST) Center for Neutron Research (NCNR). All measurements were carried out on activated samples of ≈0.8 g. At NIST, the sample was first activated via heating under dynamic vacuum at 450 K and then transferred into a He purged glove-box, loaded into a vanadium can equipped with a gas loading valve, and sealed using an indium O-ring. NPD data were collected using a Ge(311) monochromator with an in-pile 60 collimator corresponding to a wavelength of 2.0728 Å. The sample was loaded onto a closed cycle refrigerator and then data were collected at 10 K. After data collection on the activated framework, CO_2 and N_2 with different dosing levels were then loaded into the pores. The dosing levels used for CO_2 include 0.40, 1.25, and 1.60 CO_2 per Cu^{2+}, whereas for N_2 the loading levels were 0.33 and 2.19 N_2 per Cu^{2+}. For data collection, the samples were first exposed to a predetermined amount of gas at room temperature. Upon reaching an equilibrium pressure, the sample was then slowly cooled (1 K per min) to ensure complete adsorption of the CO_2 and N_2, and then data were recollected at 10 K. The resulting diffraction patterns were assessed via Le Bail and subsequent Rietveld analysis. To locate the CO_2 or N_2 molecules, Fourier difference maps were used to unveil excess scattering density in the MOF channels.

In Situ Synchrotron X-ray Diffraction. Bare and CO_2-loaded Cu−BTTri samples were measured at the Swiss-Norwegian Beamline (SNBL, BM01) at the European Synchrotron Radiation Facility (ESRF) in Grenoble, France. A custom-built in situ diffraction powder cell was designed to mount directly on the goniometer head. Before the measurements, a sample of Cu−BTTri was activated at 180 °C for 24 h. Then, both the sample and the in situ powder cell were placed into an Ar-filled glove box. Afterwards, a capillary was loaded with 2 mg of activated sample that was attached directly to the in situ cell, and then sealed using a valve. The in situ cell was subsequently removed from the glove box and mounted on the goniometer head for data collection ranging from 190 to 290 K. An Oxford Cryostream 700 with working temperature of 80−500 K was used to maintain the desired temperature. Data were collected using a DECTRIS PILATUS 2M detector and the wavelength was adjusted at 0.67522 Å. The sample to detector distance was set at 339 mm and the measurement time was varied between 20 and 40 s. After data collection of the bare framework from 190 to 290 K, the in situ cell was attached to a custom-built gas dosing manifold that is equipped with a turbo pump and pressure gauges. The Ar was evacuated from the cell, and next, the sample was dosed with 12.5 Torr of CO_2 pressurized with He to the ambient pressure. The cooling rates in all experiments were 2 K per min. The azimuthal integration of raw images was performed with the Bubble software.[21] Further, Le Bail analysis and Rietveld refinements of the acquired powder diffraction patterns were performed using TOPAS 5.[22] The CIF files for the structure of the guest loaded frameworks based on the Rietveld analysis have been produced by Topas and uploaded to the CCDC database. The table of the atomic parameters corresponding to the

https://dx.doi.org/10.1021/acs.chemmater.9b04631
Chem. Mater. 2020, 32, 1526−1536

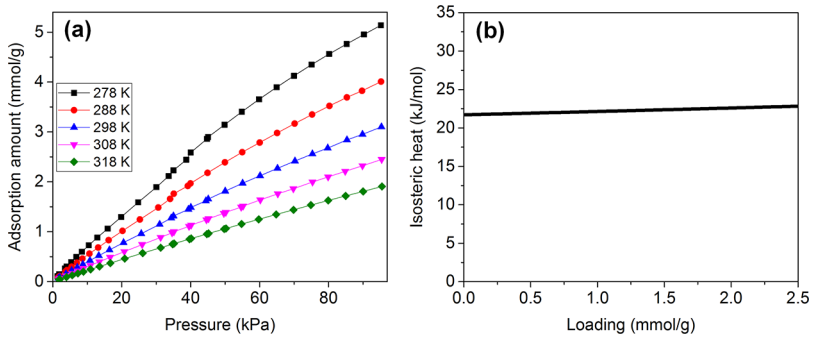

Figure 1. (a) Measured CO_2 adsorption isotherms for Cu−BTTri at different temperatures. (b) Calculated isosteric heat of CO_2 adsorption for Cu−BTTri.

bare and loaded structures has been also attached to the Supporting Information. It should be noted that, for the gas-loaded structures, the standard deviation errors related to the occupancy of guest species have been produced based on the least squares matrix of Topas. Although this is the standard procedure for the calculation of the errors associated with the occupancies in Rietveld analysis, the actual errors can deviate from the reported values.

Sequential Le Bail fitting and Rietveld analysis was carried out on the variable temperature X-ray diffraction data that ranged from 190 to 290 K for the activated sample, and the samples dosed with CO_2 or N_2. After initial analysis on the data set collected at the lowest temperature (190 K), the crystal structure obtained from Rietveld refined was used as the starting model for subsequent, sequential Le Bail/Rietveld analysis.

Electronic Structure Simulation Details. Binding energies, structural details, and charge distribution were obtained from DFT calculations, under the generalized gradient approximation by Perdew, Burke, and Ernzerhof (PBE functional).[23] All calculations were performed by using the plane-wave self-consistent field package from the Quantum Espresso[24] suite of codes. We used the following ultrasoft pseudopotentials[25] extracted from http://materialscloud.org/sssp: Cu_pbe_v1.2.uspp.F.UPF, O_pbe_v1.2.uspp.F.UPF, C_pbe_v1.2.uspp.F.UPF, H.pbe-rrkjus_psl.0.1.UPF, and N.pbe.theos.UPF. The former three were generated using the Vanderbilt code[26] and the latter two using the "atomic" code by Dal Corso.[27] We employed kinetic energy cutoffs for wave functions and charge density and potential of 55 and 660 Ry, respectively. All calculations were performed for the Γ point of the Brillouin zone because of the large size of the MOF (228 atoms in the unit cell). Spin-polarized calculations were performed to take into account the most stable spin state for Cu−BTTri, which was found to be antiferromagnetic. Following previous work[28] where other chemically similar MOFs including Cu−BTT were studied, dispersion corrections were considered under the Grimme-D2 scheme.[29] We also tested the Tkatchenko−Scheffler[30] dispersion correction scheme, and the results were found to be in good agreement with those obtained by applying the Grimme-D2 method (see the Supporting Information).

We took as a starting point the experimental configuration for Cu−BTTri, and then allowed the nuclei to relax while keeping the cell parameters fixed to experimental values (tests allowing the cell parameters to change were also carried out and have shown very small changes of 1−3% in volume). Subsequently, several calculations were set, each of them containing one gas molecule adsorbed in a different site of the MOF. We took as initial configurations those found in the experiment and allowed atomic positions to relax, again without changing the cell parameters. Binding energies were computed as the difference between the energy of the MOF/gas binary complex and the sum of the energies of MOF and gas molecule.

RESULTS AND DISCUSSION

Characterization of the Cu−BTTri Framework. The Cu−BTTri framework was first synthesized using previously published procedures[15,20] and subsequently characterized via powder X-ray diffraction to confirm the sample purity. Synchrotron X-ray diffraction data (Figure S1) reveals Bragg scattering up to a of 42° 2θ (wavelength 0.67522 Å, ≈0.94 Å d-spacing), confirming that the sample has exceptional crystallinity, a prerequisite for in situ diffraction studies. The BET surface area and the pore volume for Cu−BTTri were calculated based on the nitrogen adsorption isotherm collected at 77 K (Figure S2) to be 1850 m^2/g and 0.88 cm^3/g, respectively, which are consistent with the originally reported values for this material.[15]

We recently determined that Cu−BTTri,[20] which crystallizes in a cubic $Fm\bar{3}c$ space group (no. 226), has the following molecular formula: $Cu_3(BTTri)_2$. The structure features square $[Cu_4]^{8+}$ clusters that are interlinked by triangular $[BTTri]^{3-}$ ligands to form a neutral sodalite-type framework. The structure does not fully replicate that of its ligand-substituted counterpart, Cu−BTT,[31] or the other metal-substituted triazole analogs, such as Co−BTTri[17] and Fe−BTTri.[18] Unlike these other sodalite MOFs, the Cu−BTTri structure has no chlorine at the center of the cluster. As such, the framework is neutral and hence is devoid of any extra-framework charge-balancing species inside the channel. When compared to Co- or Fe−BTTri, the difference can be justified by the stronger Jahn−Teller distortion for octahedral copper(II) complexes, which results in the elongation of the bonds in the z-direction. Whereas in some cases this leads to the formation of distorted octahedral coordination environments,[32] in others it leads to a loss of z-bound ligands[33,34] as is the case of Cu−BTTri. When compared to Cu−BTT, the lower basicity of the tetrazolate compared to the triazolate likely helps to stabilize the presence of the Cl^- ligand. The pK_as of the triazole and tetrazole rings are approximately 13.93 and 8.23, respectively.[35] The higher basicity of $BTTri^{3-}$ implies that it is also a stronger electron donor. Consequently, the Jahn−Teller effect is more pronounced for Cu−$BTTri^{3-}$,[36] likely promoting the elimination of the chlorine in the center of square-like metal cluster. The higher ligand basicity not only influences the structural properties of the framework, but it also enhances the chemical and thermal stability of Cu−BTTri over Cu−BTT, a direct result of the higher bond strength found between the Cu and the triazolate.[15]

Standard Adsorption Isotherms and Isosteric Heat of Adsorption for CO_2 and N_2. To assess the adsorption properties of Cu−BTTri, single-component CO_2 adsorption isotherms were collected up to 1 bar and at temperatures ranging from 278 to 318 K, Figure 1a. Interestingly, the isotherm does not exhibit a steep slope in the low-pressure regime, in contrast to what is normally observed for other

https://dx.doi.org/10.1021/acs.chemmater.9b04631
Chem. Mater. 2020, 32, 1526−1536

MOFs having OMCs, such as M−BTT frameworks (Figure S3).[16] This is likely indicative of a low zero-coverage isosteric heat of CO_2 adsorption, which was extracted from the variable temperature data using a dual site Langmuir model, followed by fitting with the Clausius−Clapeyron equation (Figures 1b, S4, and S5). The zero-coverage isosteric heat was determined to be 21.7 kJ/mol for Cu−BTTri, which is significantly lower than the value previously reported for Cu−BTT, 30.7 kJ/mol.[16] This observation is not surprising, considering that $BTTri^{3-}$ is a stronger electron donor, which likely decreases the framework's affinity for CO_2 because of the lower Lewis acidity of the Cu^{2+}. It is noted that, as the CO_2 loading increases in Cu−BTTri, the isosteric heat is relatively flat. This suggests that there are other, secondary adsorption sites, which have similar isosteric heats. Further, as the pressure is increased, the interactions between neighboring CO_2 could further promote an increase in the average binding energy at constant coverage.

Nitrogen adsorption isotherms were also collected for Cu−BTTri (Figure S6) at temperatures ranging from 278 to 298 K. As expected, the amount of N_2 adsorbed in the framework is significantly less than that of CO_2, because of the lower quadrupole moment and polarizability of the N_2 compared to CO_2.[8] The weaker interaction of N_2 with the framework is further supported by the low zero-coverage isosteric heat of N_2 adsorption, which is 12 kJ/mol (Figure S7). Further, when comparing the N_2 adsorption properties of Cu−BTTri and Cu−BTT at 298 K (Figure S8), the triazole offers a lower total N_2 uptake. As such, the selectivity factors were calculated from isotherms collected at 298 K to be 27.8 and 20.8 for Cu−BTTri and Cu−BTT, respectively. The selectivity factor is the ratio of the quantity of CO_2 adsorbed at 0.15 bar/the quantity of N_2 adsorbed at 0.85 bar, normalized by the concentrations of both adsorbents. The chosen pressure points (0.15 bar for CO_2 and 0.85 bar for N_2) are those relevant to postcombustion flue gas capture. Whereas Cu−BTTri offers a higher CO_2/N_2 selectivity, Cu−BTT offers an overall higher CO_2 capacity, leaving questions as to which of these frameworks would effectively perform better in a postcombustion capture process.

Location of Adsorption Sites for CO_2 and N_2. To obtain molecular level insight into CO_2 and N_2 adsorption, neutron and synchrotron X-ray powder diffraction data were collected on the activated Cu−BTTri and then again on the sample dosed with various amounts of CO_2—0.40, 1.25, and 1.60 CO_2 per Cu^{2+}. The location and orientation of CO_2 and N_2 molecules were determined via Rietveld analysis followed by subsequent Fourier difference analysis. A total of four CO_2 adsorption sites were observed inside Cu−BTTri, which are outlined in Figure 2. Fractional atomic coordinates, occupancies, and isotropic displacement parameters for all adsorption sites are reported in Tables S6−S8, and then a comparison of experimental and computationally obtained binding energies and shortest framework distances are shown in Table S3.

The first identified CO_2 adsorption site, I, is found as expected at the OMC, Cu^{2+}. The occupancies of this adsorption site are 0.21(2), 0.74(2), and 0.82(2) for loadings of 0.40, 1.25, and 1.60 CO_2 per Cu^{2+}, respectively. $(CO_2)O\cdots Cu^{2+}$ distances range from 2.7(1) to 2.96(8) Å, depending on the CO_2 loading level (Figure 2). This results in a distance of 3.63(7) Å between the nitrogen atom of the triazole ring and the carbon atom of the CO_2. For Cu−BTT, the distance of CO_2 to the OMC was previously reported by us to be 2.60(3) Å at a loading level of 1.56 CO_2 per Cu^{2+};[16] this value is considerably shorter than the corresponding distance in Cu−BTTri, a direct result of the weaker electrostatic interaction between the metal site and the adsorbed CO_2 molecules (Figure S9). This weaker interaction is due to the reduced bonding affinity of the Cu^{2+} sites in the axial direction as a result of the more pronounced Jahn−Teller effect in Cu−BTTri compared to Cu−BTT.[28,37]

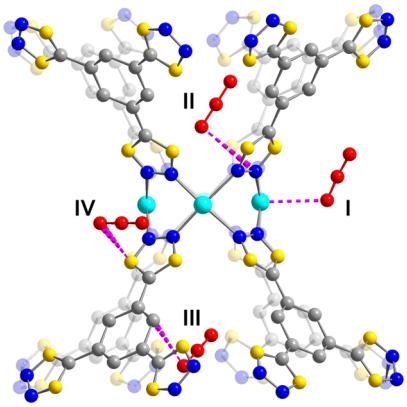

Figure 2. Ball and stick model of the Cu−BTTri framework dosed with 1.60 CO_2 per Cu^{2+}. The adsorbed CO_2 molecules are shown in red. The Cu, C, N, are denoted as cyan, gray, and blue spheres, respectively. Hydrogen atoms are excluded for the sake of clarity. Yellow spheres represent mixed sites containing both C and N. The pink dotted lines represent nearest neighbor interactions ranging from ~2.8 to 3.3 Å.

In order to obtain further insight into the mechanism of host−guest interactions in this framework, we took advantage of the theoretical support provided by DFT calculations. First, the bare Cu−BTTri and the CO_2 molecules were allowed to relax, whereas the cell parameters were kept constant (see the section on Electronic Structure Simulation Details and the Supporting Information). The distance between the OMC and CO_2 for the computationally simulated site I is 2.96 Å, which matches well with the experimentally obtained value (Table S3). Moreover, the energy of the resulting relaxed structures was computed by a single point calculation, and the binding energies were then extracted as follows (Table S3)

$$E_{\text{binding}} = E_{\text{Cu-BTTri+CO}_2} - E_{\text{Cu-BTTri}} - E_{\text{CO}_2}$$

The calculated binding energy of site I is estimated to be −25.0 kJ/mol, which matches well with the aforementioned measured zero-coverage isosteric heat of adsorption, 22 kJ/mol. To unveil the main interactions responsible for the adsorption of CO_2, the charge density difference induced by CO_2 binding was also computed. For this, the sum of the self-consistent densities for the empty Cu−BTTri framework and an isolated CO_2 molecule were first determined and then subsequently subtracted from the self-consistent density for the Cu−BTTri + CO_2 binary complex. Plots for two isosurfaces representing the charge density differences are shown in Figure S10. Based on the plot (Figure S10a) for site I, the main interactions responsible for the CO_2 binding predominantly originate from the OMC, whereas secondary interactions take place with the nitrogen atoms in the triazole ring. The charge density differences provide a qualitative indication of the perturbations induced by the CO_2 molecule on the framework, but they do not necessarily indicate the sign and magnitude of the interactions. Therefore, to better understand the mechanism of host−guest interactions at different adsorption

https://dx.doi.org/10.1021/acs.chemmater.9b04631
Chem. Mater. 2020, 32, 1526−1536

sites, decomposition of the binding energies into different contributions was carried out using the PBE functional; the results include electrostatics and short-range exchange−correlation effects. Further, the contributions dictated by van der Waals interactions were additionally computed using the Grimme-D2 method, Table S4. For the primary adsorption site, the binding energy at the DFT−PBE level is calculated to be −7.4 kJ/mol, whereas van der Waals (vdW) forces contribute a further −17.6 kJ/mol to the binding energy. Based on these results, it can be concluded that the van der Waals contribution is dominating. Most probably, the combination of the strong electron donating ligands to the Cu^{2+} OMC lends to a considerably reduced electrostatic affinity toward the guest species when compared to Cu−BTT.[16,28] For other MOFs with OMCs, like HKUST-1 and MOF-74, contributions to CO_2 binding are mainly attributed to strong electrostatic interactions.[38] For Cu−BTTri, the highly electron donating ligand can reduce the charge, and hence electrostatic contribution at the OMC.[20] It is noted that whereas vdW interactions are the dominant force found in Cu−BTTri, electrostatic interactions, and other terms that are well-described at the DFT−PBE level, also play an important role in the overall binding energy.

The second CO_2 adsorption site, II, located just above the metal cluster (Figure 2), is disordered around the fourfold rotation axis that passes through the center of the square-like metal cluster; this static disorder is dictated by vdW interactions between this CO_2 and the ligand. The shortest distance is 3.27(4) Å, which is found between the oxygen atom of the CO_2 molecule and the nitrogen atom on the triazole ring. Within the error of the experimental data, the DFT-based simulations provide a secondary adsorption site that is nearly identical to site II. The shortest framework−CO_2 distance is approximately 3.16 Å. Like site I, site II can be observed in all refined structures regardless of the CO_2 loading. The occupation of this adsorption site ranges from 0.101(6) at the loading of 0.40 CO_2 per Cu^{2+} and reaches a value of 0.67(3) at the highest loading of 1.60 CO_2 per Cu^{2+}. The fact that the occupancies for site I and II are similar indicates that the enthalpy of adsorption for these sites are also comparable, a hypothesis that is further supported by the linear isosteric heat of CO_2 adsorption obtained from Cu−BTTri (Figure 1b). This is also confirmed by DFT calculations that yield a value of −26.5 kJ/mol for the isosteric heat of adsorption of site II, which is only 1.5 kJ/mol higher than that of site I (Table S3). The isosurface plot for site II confirms the interaction between the electron-rich triazole groups with the CO_2 molecule. Moreover, DFT calculations show that binding in this site is entirely due to strong vdW interactions ($E_{\text{dispersion-D2}}$ = −30.3 kJ/mol), with a repulsive interaction between the host framework and the adsorbed CO_2 at the DFT−PBE level (E_{PBE} = +3.8 kJ/mol, see Table S4). This can probably be explained by electrostatics, because both moieties, including the triazole rings and oxygen atom of the carbon dioxide molecule, have a surplus of partial negative charge.

The third CO_2 adsorption site, site III, is located nearest to the benzene rings on the ligand (see Figure 2).[16] The main mechanism for the stabilization of this adsorption site is through vdW interactions between the oxygen atom of the CO_2 with the carbon atoms of the benzene ring. The shortest framework distance for site III is 2.8(1) Å, which is similar to other vdW interactions found between CO_2 and other MOFs.[39−41] DFT calculations have also successfully modeled this adsorption site and predicted its binding energy to be −17.0 kJ/mol, which is lower than those calculated for site II (Table S4). This observed drop in binding energy is consistent with the observation that the relative occupancy of site III is significantly lower than sites I and II at all CO_2 loadings evaluated. For example, at the highest loading, 1.60 CO_2 per Cu^{2+}, the occupancy of site III is 0.124(8), whereas sites I and II are 0.82(2) and 0.67(3), respectively. Despite the lower predicted binding energy of site III, the simulated site III binding energy might not be precise, because the DFT calculations do not take intermolecular CO_2−CO_2 interactions into account. The shortest contact distance for site III is approximately 3 Å from site II CO_2 and hence, this likely implies that the adsorption is further stabilized by intermolecular CO_2(II)−CO_2(III) interactions. The importance of these intermolecular interactions also explains the very low occupancy of site III at lower CO_2 loadings. It should be noted that, unlike sites I and II, there are more pronounced differences between the experimental and DFT-determined location of site III CO_2 (see Table S3), which can be attributed to the fact that only a single adsorbed CO_2 molecule is considered in the DFT calculations.

The fourth adsorption site, IV, was found inside the large pore of Cu−BTTri, at the same location where the extra cations and anions were previously observed in Cu−BTT (Figure 2).[16] Site IV is in close proximity to the triazole ring, with the shortest framework−CO_2 distance equal to 3.02(9) Å. This adsorption site has additional interactions with other atoms of the triazole ring with distances that range from ∼3 to 3.5 Å. The DFT-determined binding energy for site IV is −15.8 kJ/mol, almost entirely due to vdW interactions ($E_{\text{dispersion-D2}}$ = −15.8 kJ/mol and E_{PBE} = +0.05 kJ/mol). The latter could result from a minimal interaction with the Cu^{2+}, consisted with a distance of approximately 4.6 Å between site IV and the OMC. This is no surprise given the long distance combined with the low Lewis acidity of Cu^{2+} in this structure.

In order to further understand the performance of the material for CO_2/N_2 separations in Cu−BTTri, the N_2 adsorption sites were also determined via Rietveld analysis of neutron diffraction data dosed with the 0.33 and 2.19 N_2 per Cu^{2+}. This analysis has led to the elucidation of six adsorption sites, I−VI, shown in Figure 3.

The first N_2 adsorption site is found at the OMC, with a Cu^{2+}−N_2 distance of 2.74(5) Å (Figure 3). The occupancy of site I N_2 is 0.145(7) and 0.326(8) at loadings of 0.33 and 2.19 N_2 per Cu^{2+}, respectively. The binding energy for this adsorption site is calculated to be −11.9 kJ/mol, which is in excellent agreement with the zero-coverage isosteric heat of adsorption (Q_{st} = 11.9 kJ/mol) obtained from variable temperature N_2 adsorption isotherms collected from 278 to 298 K. The contribution of vdW and DFT−PBE terms have been calculated to be −9.9 and −2.0 kJ/mol, respectively.

The energy decomposition based on DFT + vdW calculations can help understand better the role of the physicochemical properties of the adsorbate on the nature and extent of the host−guest interaction. Whereas the DFT−PBE baseline involves many other terms, for example, Pauli repulsion and exchange−correlation energy, it largely reflects electrostatic interactions between the adsorbate and the framework. For instance, in our previous work,[20] we demonstrated that DFT−PBE interactions between the OMC and D_2 molecule are responsible for less than 5% of the total binding energy, whereas in this work the share is

https://dx.doi.org/10.1021/acs.chemmater.9b04631
Chem. Mater. 2020, 32, 1526−1536

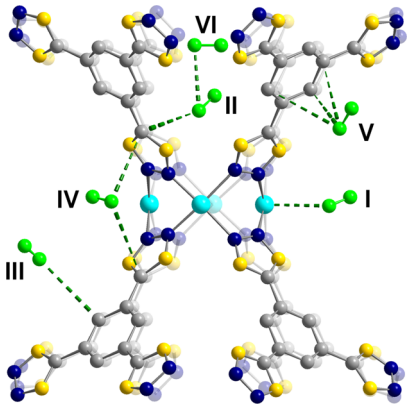

Figure 3. Ball and stick model of the Cu−BTTri framework dosed with 2.19 N_2/Cu^{2+}. The adsorbed N_2 molecules are depicted in green. The Cu, C, N, are denoted as cyan, gray, and blue spheres, respectively. Hydrogen atoms are excluded for the sake of clarity. Yellow spheres represent atomic sites that are mixed with both C and N. The green dotted lines represent nearest neighbor interactions, and have distances ranging from 2.74(5) to 3.67(5) Å.

calculated to be approximately 17 and 31% for N_2 and CO_2, respectively (Tables S4 and S5). The electrostatic nature of these interactions is consistent with the relation between their magnitude and that of the adsorbate's permanent multipoles.[20] For example, CO_2, N_2, and H_2 have quadrupole moments of 43.0 × 10^{-27}, 15.2 × 10^{-27}, and 6.6 × 10^{-27} $esu^{-1}.cm^{-1}$, respectively,[8] that follow the same trend as the DFT−PBE binding energies of CO_2, N_2, and H_2, that is −7.41, −1.98, and −0.49 kJ/mol, respectively. For the gases with stronger permanent multipoles, tuning the charge in the framework wall can have a larger impact on the adsorption properties, whereas for those with weaker or no permanent multipole, the vdW interaction tends to dominate.[20] Understanding this relationship can provide insight into how to alter the structural features to optimize the adsorbate's physicochemical properties for different separations.

The second N_2 adsorption site, II, is located just above the Cu_4^{8+} cluster, albeit slightly farther away from the cluster than observed for CO_2 (Figure 3). Like I, site II N_2 can be detected in the data obtained from 0.33 and 2.19 N_2 per Cu^{2+} loadings with occupancies of 0.020(4) and 0.149(8), respectively. The shortest distance, 3.21(9) Å, is found between a framework carbon atom and site II N_2 (Figure 3). This interaction is predominantly vdW in nature, and this is further corroborated by the calculated shares of vdW and DFT−PBE interactions as well as the charge difference isosurface plot (Table S5 and Figure S11). The other four N_2 adsorption sites, III to VI, only appear in the diffraction data collected at the highest N_2 loading, 2.19 N_2 per Cu^{2+}. These sites have occupancies ranging from 0.296(9) to 0.020(5) and all exhibit N_2-framework distances greater than 3 Å with DFT calculated binding energies that range from −4.5 to −7.1 kJ/mol. Whereas site VI is not found in close proximity to the framework wall, there are N_2−N_2 intermolecular interactions with site II, which likely help to stabilize the last adsorption site.

When comparing Cu−BTTri to Cu−BTT, the total N_2 uptake at room temperature of the former is significantly lower at pressures below 1 bar (Figure S8). Considering the low-pressure regime is typically dominated by the strongest adsorption sites, we surmise that the low N_2 adsorption of Cu−BTTri stems from sites I and II. Obviously, the OMC in Cu−BTTri has a lower Lewis acidity reducing N_2 adsorption at low pressures. Moreover, for the second adsorption site, the triazole rings have a high partial negative charge that destabilizes N_2 adsorption (check the electrostatic contribution at Table S5). Given the higher basicity of the triazole ligand, it is hypothesized that such a destabilizing interaction would be sufficiently smaller for the tetrazole, making N_2 binding in site II stronger. Therefore, the presence of weaker primary and secondary binding sites in the triazole framework is an explanation for the material's significantly lower N_2 adsorption when compared to Cu−BTT.

Evolution of Lattice Parameters and Guest Occupancies as a Function of Temperature. In addition to CO_2 and N_2 binding, the bulk properties of the material, such as unit cell parameters and cell volume, were investigated as a function of temperature and gas loading level. This allows us to follow adsorption/desorption processes and better understand how the material's structure changes as a function of external stimuli. In this work, in situ synchrotron X-ray diffraction measurements were employed rather than neutron diffraction, in order to obtain rapid measurements using small sample sizes. First, data were collected at 100 K on a Cu−BTTri sample dosed with 12.5 Torr of CO_2 (1.09 CO_2/Cu^{2+}) as it was necessary to determine if the position of CO_2 could be elucidated via synchrotron X-ray diffraction. Indeed, Rietveld analysis permitted the elucidation of the same four adsorption sites (Table S11) as observed via NPD. Afterward, variable temperature measurements were performed on the activated sample and then again on the aforementioned sample dosed with 12.5 Torr of CO_2 gas. For both samples, data were collected during cooling from 290 to 190 K (rate of 2 K per min). For the bare Cu−BTTri, Figure 4, the lattice parameter *a*

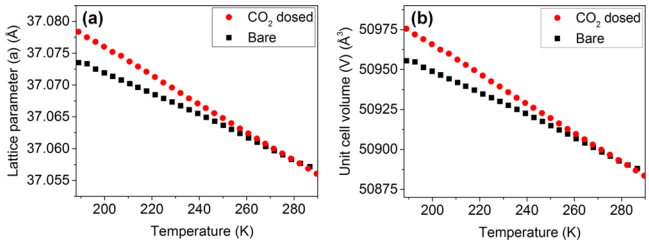

Figure 4. Change of (a) lattice parameter (*a*) (b) unit cell volume (*V*) of activated Cu−BTTri with temperature.

increases from 37.0571(1) to 37.0735(1) Å upon cooling, which leads to an increase in cell volume by 0.13%, representative of negative thermal expansion (NTE). The average thermal expansion coefficient, α, was calculated for the lattice parameter *a*, to be approximately −4.5 $(MK)^{-1}$. Albeit small, NTE was previously reported for only a few MOF structures to date.[42−44] This magnitude of NTE behavior for this framework is similar to what was observed for HKUST-1, a well-known cubic MOF structure that has an average thermal expansion coefficient of −4.1 $(MK)^{-1}$.[44] Understanding the extent to which a material contracts or expands as a function of temperature is important to better understand how it might change throughout the course of a separation, a factor that can significantly impact process engineering. Interestingly, the NTE becomes even more pronounced when the sample is under 12.5 Torr of CO_2. Upon decreasing the temperature from 290 to 190 K, the lattice parameter, *a*, increases from

https://dx.doi.org/10.1021/acs.chemmater.9b04631
Chem. Mater. 2020, 32, 1526−1536

37.0560(1) to 37.0783(1) Å and results in a 0.18% change in the unit cell volume, this leads to a slightly larger thermal expansion coefficient, α, of −6.0 $(MK)^{-1}$ (Figure 4). The more intense NTE in the presence of CO_2 gas can be attributed to the development of host−guest interactions inside the framework as the amount of loaded adsorbate increases upon decreasing temperature. Similar behavior was previously reported for Fe_2(dobdc) and Mg_2(dobdc),[45] where an increase in CO_2 dosing led to the increase in the degree of the lattice expansion for the framework.[37]

Subsequent to the unit cell analysis, carried out via LeBail fitting, sequential Rietveld analysis was performed on the aforementioned variable temperature diffraction data obtained from Cu−BTTri dosed with 1.09 CO_2 per Cu^{2+}. The occupancies of sites I−IV are plotted as a function of temperature in Figure 5. Whereas the occupancies of site III

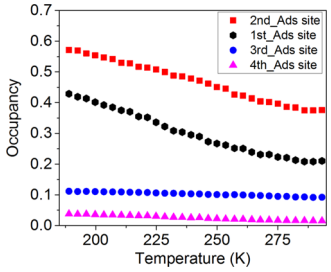

Figure 5. Occupation of different CO_2 adsorption sites in Cu−BTTri as a function of temperature.

and site IV are minimal over the entire temperature regime, the occupancies of sites I and II increase significantly as the temperature is decreased, which is due to the higher isosteric heats of CO_2 adsorption, as predicted by the van't Hoff equation.[46] Further, it is noted that at these temperatures, the second adsorption, site II, has a higher occupancy than site I, which is counterintuitive to the observations seen via NPD data collected at 10 K, which shows a higher occupancy of site I over site II. The occupancies are 0.21(1) and 0.38(1) at the highest temperature, 290 K, whereas the occupancies increase to 0.43(1) and 0.57(1), for sites I and II respectively, at 190 K. Whereas an energy difference as small as ≈3 kJ/mol is sufficient to cause a sequential occupation of adsorption sites at 10 K, at higher temperatures, where adsorption isotherms are collected, it is possible that the distribution of the occupancies is also influenced by entropic effects.[47] Therefore, despite the higher occupancy of site II at room temperature, it is still assumed that site I is energetically favorable, and hence has a higher occupancy at temperatures approaching 0 K where entropy effects are highly attenuated.

Transient Breakthrough Simulations in Fixed Bed Adsorbers. Given that the single-component adsorption isotherms imply that Cu−BTTri has a higher selectivity for CO_2 over N_2, whereas Cu−BTT has a higher CO_2 capacity, it was of interest to evaluate the potential of these frameworks in a dry postcombustion capture process (see scheme in Figure 6). For a clear comparison, Figure 7a shows the adsorption selectivities of Cu−BTT and Cu−BTTri over the whole pressure range and Figure 7b compares the volumetric CO_2 uptake capacities of both Cu−BTT and Cu−BTTri. We note that Cu−BTT has an uptake capacity that is significantly higher than Cu−BTTri by a factor of 2, despite the higher selectivity for the latter.

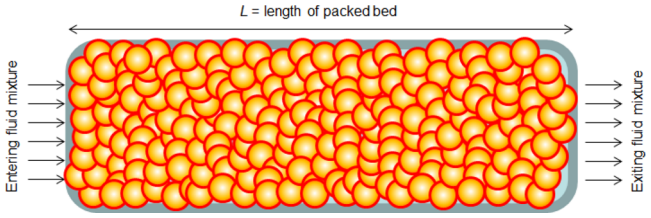

Figure 6. Schematic figure of a fixed bed adsorption bed for the postcombustion capture process.

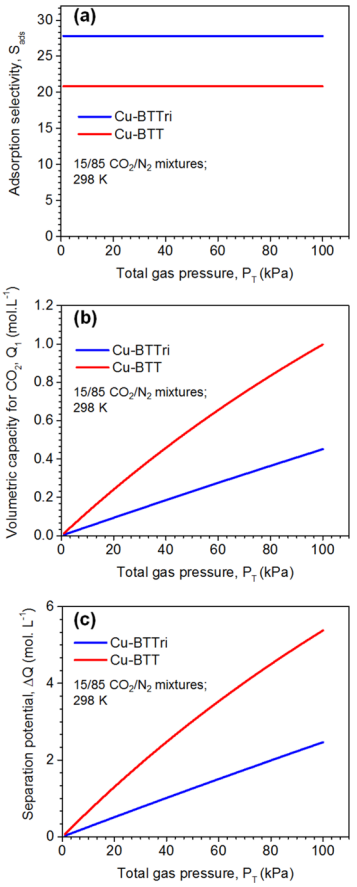

Figure 7. (a) Adsorption selectivity (S_{ads}), (b) volumetric capacity for CO_2, Q_1, and (c) separation potential, ΔQ, as a function of total pressure.

The typical composition of the flue gas feed is approximately 15/85 v/v CO_2/N_2 and the separations are normally carried out in fixed bed adsorbers (see schematic in Figure 6); such adsorbers are commonly operated in transient mode, and the compositions of the gas phase, as well as component loadings within the crystals, vary with position and time.[48−50] During the initial stages of the transience, the pores are gradually loaded, and only toward the end of the adsorption cycle is pore saturation attained. For a given separation task, transient breakthroughs provide a more realistic evaluation of the efficacy of a material, as they reflect the combined influence of CO_2/N_2 adsorption selectivity and CO_2 uptake capacity.[49,50]

The adsorption selectivity is defined by

$$S_{ads} = \frac{q_1/q_2}{y_1/y_2} \quad (1)$$

https://dx.doi.org/10.1021/acs.chemmater.9b04631
Chem. Mater. 2020, 32, 1526−1536

where the q_1 and q_2 represent the molar loadings of $CO_2(1)$ and $N_2(2)$ within the MOF that is in equilibrium with a bulk fluid mixture with mole fractions y_1 and $y_2 = 1 - y_1$. The molar loadings, also called gravimetric uptake capacities, are usually expressed with the units mol kg^{-1}. The component loadings are commonly calculated on the basis of unary isotherm data fits, along with the ideal adsorbed solution theory (IAST) of Myers and Prausnitz[51] for mixture adsorption equilibrium (see the Supporting Information). The volumetric uptake capacities are

$$Q_1 = \rho q_1; \qquad Q_2 = \rho q_2 \tag{2}$$

where ρ is the crystal framework density of the MOF, expressed in units of kg m^{-3}, or kg L^{-1}.

High uptake capacities are desirable because these result in longer breakthrough times and reduced frequency of bed regeneration. Higher values of S_{ads} are also desired because they lead to sharper breakthrough fronts and larger differences between the breakthrough times of individual constituents. If high product purities are desired, then this also demands $S_{ads} \gg 1$. Most commonly, however, high uptake capacities do not go hand-in-hand with high selectivities.[50,52]

In order to overcome the selectivity/capacity trade-off for these two MOFs, we adopted an approach previously developed by Krishna,[52] which defines a combined selectivity/capacity metric that is derived using the "shock wave" model for fixed bed adsorbers. The maximum achievable productivity of purified N_2 is realized when both intracrystalline diffusion and axial dispersion effects are completely absent and the concentrations "fronts" of the fluid mixture traverse the fixed bed in the form of shock waves.[52] For the separation of $CO_2(1)/N_2(2)$ mixtures, the maximum achievable productivity, ΔQ, called the separation potential, can be calculated using the shock-wave model; the result is[52]

$$\Delta Q = Q_1 \frac{y_2}{1 - y_2} - Q_2 \tag{3}$$

The quantity ΔQ can be described as an appropriate combination of selectivity and uptake capacity that is reflective of the separation potential for a specific adsorbent in a fixed bed.[52] The ΔQ, expressed in moles of N_2 per L of adsorbent, represents the maximum amount of pure N_2 that can be recovered during the adsorption phase of the fixed bed separation and hence, is also indicative of the amount of CO_2 that is adsorbed on the bed until the point of breakthrough. Of course, it should be noted that if the purity of the CO_2 gas, which is released in the desorption stage, is of utmost importance, then the evaluation of the materials may be done based on the selectivity rather than separation potential.

A comparison of the separation potential, ΔQ, of Cu−BTT and Cu−BTTri for 15/85 $CO_2(1)/N_2(2)$ mixtures at 298 K, is plotted as a function of the total pressure, p_t in Figure 7c. At 100 kPa total pressure, the ΔQ is 5.4 mol·L^{-1} for Cu−BTT and 2.7 2.7 mol L^{-1} for Cu−BTTri. These values imply that Cu−BTT has the potential to produce twice the amount of pure N_2 as Cu−BTTri. In order to confirm the superior performance of Cu−BTT, transient breakthrough curves were also simulated for 15/85 CO_2/N_2 gas mixtures at an operating pressure of 100 kPa and 298 K using a methodology reported previously.[49,50,52,53] For the breakthrough simulations, the following parameter values were used: length of packed bed, L = 0.3 m; voidage of packed bed, ε = 0.4; superficial gas velocity at inlet, u = 0.04 m/s.

The results for the transient breakthrough simulations obtained from a fixed bed packed with (a) Cu−BTT and (b) Cu−BTTri are shown in Figure 8. The transient

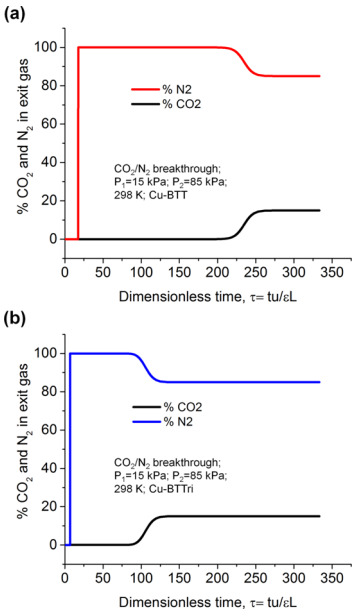

Figure 8. Transient CO_2 and N_2 breakthrough curves for (a) Cu−BTT and (b) Cu−BTTri frameworks.

breakthrough simulation results are presented in terms of a dimensionless time as the x-axis, τ, defined by dividing the actual time, t, by the characteristic time, $L\varepsilon/u$. The y-axis represents the % CO_2 and % N_2 in the gas mixture exiting the adsorber. The time at which CO_2 "breaks through" is significantly higher for Cu−BTT, as compared to Cu−BTTri; this can be primarily ascribed to the higher CO_2 capacity of Cu−BTT, as shown in Figure 7b. During the time interval indicated by $\Delta\tau$ in Figure 8, nearly pure N_2 can be produced. Note that the time interval $\Delta\tau$ is higher for Cu−BTT than that of Cu−BTTri by nearly a factor of 2. Arbitrarily setting the minimum purity requirements for N_2 as 99.95%, we can determine the productivity of N_2 from a material balance on the adsorber. The calculated values for Cu−BTT and Cu−BTTri are, respectively, 4.3 and 1.8 mol L^{-1}, confirming that the separations with Cu−BTT yield a significantly higher productivity of pure N_2 and thus a higher amount of CO_2 can be captured. The actual values of the productivities for Cu−BTT and Cu−BTTri are lower than the corresponding values of ΔQ, calculated using the IAST (see Figure 7c), because of the distended nature of the transient breakthroughs in Figure 8.

Overall, neither the adsorption capacity of the single gases nor the selectivity, S_{ads}, is a proper metric for judging the effectiveness of a specific MOF for separations in fixed bed adsorbers. Separation potential can give a better estimation of how effective a material's performance is. However, depending on the particular requirements for each case, such as CO_2 recovery, CO_2 purity, or the effective amount of gas captured per mass unit of the material, the final choice might be different. For example, in the present case, for optimizing CO_2 recovery, Cu−BTT is a better option because it yields higher

https://dx.doi.org/10.1021/acs.chemmater.9b04631
Chem. Mater. 2020, 32, 1526−1536

amount of cyclic CO_2 adsorption because of its higher separation potential. However, if the CO_2 purity is the main target, Cu−BTTri, which shows better CO_2/N_2 selectivity, would be a better choice for this separation.

CONCLUSIONS

This work presents a comprehensive study of CO_2 and N_2 adsorption in a sodalite MOF known as Cu−BTTri; this was carried out using a series of characterization tools including single-component adsorption measurements, in situ neutron and X-ray diffraction, DFT calculations, and finally breakthrough simulations. Whereas CO_2 and N_2 isotherms are used to assess selectivity and adsorption capacity, in situ diffraction is used to provide molecular level insight into the location and orientation of these two small molecules throughout the framework. As such, the diffraction technique allows further rationalization of the observed isotherms, provides a means to monitor adsorption/desorption processes, and allows one to assess changes in the framework as a function of temperature. Albeit small, both the activated and CO_2-loaded Cu−BTTri are found to exhibit a rare NTE phenomenon, with average thermal expansion coefficients of −4.5 and −6.0 $(MK)^{-1}$, respectively. In addition, DFT calculations are used to predict the binding energies and geometries of potential adsorption sites, results which are found to be in good agreement with those determined experimentally. To better understand the host−guest interaction at each adsorption site, the calculated binding energies were further decomposed into separate contributions from DFT−PBE (predominantly electrostatic) and van der Waals interactions.

Finally, the performance of Cu−BTTri is compared to a ligand-substituted counterpart, Cu−BTT. While the sodalite structures are similar, the ligand exchange has an extreme effect on the performance of the material with regard to CO_2 and N_2 adsorption. Despite that Cu−BTTri exhibits a lower overall adsorption capacity and weaker interactions with both CO_2 and N_2, the material surprisingly offers a higher selectivity for CO_2 over N_2 compared to that of its tetrazole counterpart. These results stem from the fact that the triazolate offers a stronger Cu−ligand bond compared to the tetrazolate, and hence, significantly weakens the interactions along the *z*-axis, where small molecules bind. This assumption is validated by neutron diffraction and adsorption measurements, which show elongated Cu−CO_2 distances and lower initial isosteric heats of CO_2 adsorption, respectively. We finally compared these materials' performance in a dry, postcombustion flue gas separation. For this, the separation potential, ΔQ, of Cu−BTT and Cu−BTTri was determined, and transient breakthrough curves were simulated; it was concluded that, despite its higher selectivity for CO_2 over N_2, Cu−BTTri does not outperform Cu−BTT for the separation of interest. It was demonstrated that adsorption capacity and selectivity alone cannot be appropriate metrics to evaluate the efficiency of an adsorbent to be employed in a chosen separation.

It should be reiterated that this study is based on the thermodynamic and hydrodynamic properties of the frameworks of interest in dry postcombustion capture conditions. For the actual application of a material in such a large-scale separation, other techno-economic factors like price, long-term stability/cyclability, ease of regeneration, temperature spikes during adsorption, and the influence of water and minor impurities, like SO_x and NO_x, must also be considered.

ASSOCIATED CONTENT

Supporting Information

The Supporting Information is available free of charge at https://pubs.acs.org/doi/10.1021/acs.chemmater.9b04631.

Experimental neutron and synchrotron powder X-ray diffraction patterns, calculated diffraction patterns obtained by Rietveld analysis and Fourier difference patterns, nitrogen adsorption measurements, BET surface area calculations, carbon dioxide measurements, fit of experimental gas adsorption data by Langmuir and dual-site Langmuir model, experimental and computational CO_2 and N_2 gas adsorption measurements, experimental and computational shortest framework distance for different individual adsorption sites, computational decomposition of electrostatic and vdW interactions, and isosurfaces of the charge density plots (PDF)

CuBTTr_NPD_0_5_CO2_10K crystallographic data (CIF)

CuBTTr_NPD_0_5_N2_10K crystallographic data (CIF)

CuBTTr_NPD_1_5_CO2_10K crystallographic data (CIF)

CuBTTr_NPD_2_5_CO2_10K crystallographic data (CIF)

CuBTTr_NPD_1_5_N2_10K crystallographic data (CIF)

CuBTTri_1_CO2_Cu_synchrotron crystallographic data (CIF)

CO2_SITE1_DFT data (XYZ)

CO2_SITE2_DFT data (XYZ)

CO2_SITE3_DFT data (XYZ)

CO2_SITE4_DFT data (XYZ)

N2_SITE1_DFT data (XYZ)

N2_SITE2_DFT data (XYZ)

N2_SITE3_DFT data (XYZ)

N2_SITE4_DFT data (XYZ)

N2_SITE5_DFT data (XYZ)

N2_SITE6_DFT data (XYZ)

AUTHOR INFORMATION

Corresponding Author

Wendy L. Queen − *Institut des Sciences et Ingenierie Chimiques, Ecole Polytechnique Fédérale de Lausanne (EPFL), CH-1951 Sion, Switzerland;* orcid.org/0000-0002-8375-2341; Email: wendy.queen@epfl.ch

Authors

Mehrdad Asgari − *Institut des Sciences et Ingenierie Chimiques, Ecole Polytechnique Fédérale de Lausanne (EPFL), CH-1951 Sion, Switzerland*

Rocio Semino − *Institut Charles Gerhardt Montpellier UMR 5253 CNRS, Université de Montpellier, 34095 Montpellier Cedex 05, France; Laboratory of Computational Science and Modeling, Institute of Materials, Ecole Polytechnique Fédérale de Lausanne, 1015 Lausanne, Switzerland;* orcid.org/0000-0003-3937-7414

Pascal A. Schouwink − *Institut des Sciences et Ingenierie Chimiques, Ecole Polytechnique Fédérale de Lausanne (EPFL), CH-1951 Sion, Switzerland*

https://dx.doi.org/10.1021/acs.chemmater.9b04631
Chem. Mater. 2020, 32, 1526−1536

Ilia Kochetygov − *Institut des Sciences et Ingenierie Chimiques, Ecole Polytechnique Fédérale de Lausanne (EPFL), CH-1951 Sion, Switzerland*

Jacob Tarver − *Center for Neutron Research, National Institute of Standards and Technology, 20899 Gaithersburg, Maryland, United States; National Renewable Energy Laboratory, 80401 Golden, Colorado, United States*

Olga Trukhina − *Institut des Sciences et Ingenierie Chimiques, Ecole Polytechnique Fédérale de Lausanne (EPFL), CH-1951 Sion, Switzerland*

Rajamani Krishna − *Van 't Hoff Institute for Molecular Sciences, University of Amsterdam, 1098 XH Amsterdam, Netherlands;* orcid.org/0000-0002-4784-8530

Craig M. Brown − *Center for Neutron Research, National Institute of Standards and Technology, 20899 Gaithersburg, Maryland, United States*

Michele Ceriotti − *Laboratory of Computational Science and Modeling, Institute of Materials, Ecole Polytechnique Fédérale de Lausanne, 1015 Lausanne, Switzerland;* orcid.org/0000-0003-2571-2832

Complete contact information is available at: https://pubs.acs.org/10.1021/acs.chemmater.9b04631

Notes

The authors declare no competing financial interest.

■ ACKNOWLEDGMENTS

This work was supported by the Swiss National Science Foundation under grant PYAPP2_160581 and the Swiss Commission for Technology and Innovation (CTI). C.M.B. was supported through the Center for Gas Separations Relevant to Clean Energy Technologies, an Energy Frontier Research Center funded by the U.S. Department of Energy, Office of Science, Office of Basic Energy Sciences under Award DE-SC0001015. We acknowledge BT1 beamline at the National Institute of Standards and Technology (NIST) Center for Neutron Research (NCNR) for beamtime allocation. We also acknowledge the Swiss-Norwegian Beam Line BM01 at European Synchrotron Radiation Facility (ESRF) for beamtime allocation and Dr. Dmitry Chernyshov and Dr. Iurii Dovgaliuk for their assistance on the beamline. J.T. gratefully acknowledges research support from the U.S. Department of Energy, Office of Energy Efficiency and Renewable Energy, Fuel Cell Technologies Office, under Contract no. DE-AC36- 08GO28308. R.S. and M.C. acknowledge the support of the Swiss National Supercomputing Centre (CSCS) by means of a grant under project ID s887. M.A. and R.S. thank financial support provided by SCCER Efficiency of Industrial Processes. O.T. is financially supported by the National Center for Competence in Research (NCCR) "Materials' Revolution:Computational Design and Discovery, of Novel Materials (MARVEL)" of the Swiss National Science Foundation (SNSF) and EPFL Fellows co-funded by Marie Skłodowska-Curie.

■ REFERENCES

(1) Van Groenigen, K. J.; Qi, X.; Osenberg, C. W.; Luo, Y.; Hungate, B. A. Faster decomposition under increased atmospheric CO2 limits soil carbon storage. *Science* **2014**, *344*, 508−509.

(2) Beleggia, R.; Fragasso, M.; Miglietta, F.; Cattivelli, L.; Menga, V.; Nigro, F.; Pecchioni, N.; Fares, C. Mineral composition of durum wheat grain and pasta under increasing atmospheric CO2 concentrations. *Food Chem.* **2018**, *242*, 53−61.

(3) Drage, T. C.; Snape, C. E.; Stevens, L. A.; Wood, J.; Wang, J.; Cooper, A. I.; Dawson, R.; Guo, X.; Satterley, C.; Irons, R. Materials challenges for the development of solid sorbents for post-combustion carbon capture. *J. Mater. Chem.* **2012**, *22*, 2815−2823.

(4) Mason, J. A.; Sumida, K.; Herm, Z. R.; Krishna, R.; Long, J. R. Evaluating metal-organic frameworks for post-combustion carbon dioxide capture via temperature swing adsorption. *Energy Environ. Sci.* **2011**, *4*, 3030−3040.

(5) Samanta, A.; Zhao, A.; Shimizu, G. K. H.; Sarkar, P.; Gupta, R. Post-combustion CO2 capture using solid sorbents: a review. *Ind. Eng. Chem. Res* **2011**, *51*, 1438−1463.

(6) Mason, J. A.; McDonald, T. M.; Bae, T.-H.; Bachman, J. E.; Sumida, K.; Dutton, J. J.; Kaye, S. S.; Long, J. R. Application of a high-throughput analyzer in evaluating solid adsorbents for post-combustion carbon capture via multicomponent adsorption of CO2, N2, and H2O. *J. Am. Chem. Soc.* **2015**, *137*, 4787−4803.

(7) Stylianou, K. C.; Queen, W. L. Recent Advances in Carbon Capture with Metal-Organic Frameworks. *CHIMIA Int. J. Chem.* **2015**, *69*, 274−283.

(8) Li, L.; Wong-Ng, W.; Huang, K.; Cook, L. P. *Materials and Processes for CO_2 Capture, Conversion, and Sequestration*; John Wiley & Sons: Hoboken, 2018.

(9) Férey, G. Hybrid porous solids: past, present, future. *Chem. Soc. Rev.* **2008**, *37*, 191−214.

(10) Zhang, Z.; Yao, Z.-Z.; Xiang, S.; Chen, B. Perspective of microporous metal−organic frameworks for CO_2 capture and separation. *Energy Environ. Sci.* **2014**, *7*, 2868−2899.

(11) Zuluaga, S.; Canepa, P.; Tan, K.; Chabal, Y. J.; Thonhauser, T. Study of van der Waals bonding and interactions in metal organic framework materials. *J. Phys.: Condens. Matter* **2014**, *26*, 133002.

(12) Pettinari, C.; Tăbăcaru, A.; Galli, S. Coordination polymers and metal−organic frameworks based on poly (pyrazole)-containing ligands. *Coord. Chem. Rev.* **2016**, *307*, 1−31.

(13) Aromí, G.; Barrios, L. A.; Roubeau, O.; Gamez, P. Triazoles and tetrazoles: Prime ligands to generate remarkable coordination materials. *Coord. Chem. Rev.* **2011**, *255*, 485−546.

(14) Howarth, A. J.; Liu, Y.; Li, P.; Li, Z.; Wang, T. C.; Hupp, J. T.; Farha, O. K. Chemical, thermal and mechanical stabilities of metal−organic frameworks. *Nat. Rev. Mater.* **2016**, *1*, 15018.

(15) Demessence, A.; D'Alessandro, D. M.; Foo, M. L.; Long, J. R. Strong CO2 binding in a water-stable, triazolate-bridged metal−organic framework functionalized with ethylenediamine. *J. Am. Chem. Soc.* **2009**, *131*, 8784−8786.

(16) Asgari, M.; Jawahery, S.; Bloch, E. D.; Hudson, M. R.; Flacau, R.; Vlaisavljevich, B.; Long, J. R.; Brown, C. M.; Queen, W. L. An experimental and computational study of CO 2 adsorption in the sodalite-type M-BTT (M= Cr, Mn, Fe, Cu) metal−organic frameworks featuring open metal sites. *Chem. Sci.* **2018**, *9*, 4579−4588.

(17) Xiao, D. J.; Gonzalez, M. I.; Darago, L. E.; Vogiatzis, K. D.; Haldoupis, E.; Gagliardi, L.; Long, J. R. Selective, tunable O2 binding in cobalt (II)−triazolate/pyrazolate metal−organic frameworks. *J. Am. Chem. Soc.* **2016**, *138*, 7161−7170.

(18) Reed, D. A.; Xiao, D. J.; Gonzalez, M. I.; Darago, L. E.; Herm, Z. R.; Grandjean, F.; Long, J. R. Reversible CO scavenging via adsorbate-dependent spin state transitions in an iron (II)−triazolate metal−organic framework. *J. Am. Chem. Soc.* **2016**, *138*, 5594−5602.

(19) Shearer, G. C.; Colombo, V.; Chavan, S.; Albanese, E.; Civalleri, B.; Maspero, A.; Bordiga, S. Stability vs. reactivity: understanding the adsorption properties of Ni 3 (BTP) 2 by experimental and computational methods. *Dalton Trans.* **2013**, *42*, 6450−6458.

(20) Asgari, M.; Semino, R.; Schouwink, P.; Kochetygov, I.; Trukhina, O.; Tarver, J. D.; Bulut, S.; Yang, S.; Brown, C. M.; Ceriotti, M.; Queen, W. L. An in-situ neutron diffraction and DFT study of hydrogen adsorption in a sodalite-type metal−organic framework, Cu-BTTri. *Eur. J. Inorg. Chem.* **2019**, *2019*, 1147−1154.

(21) Dyadkin, V.; Pattison, P.; Dmitriev, V.; Chernyshov, D. A new multipurpose diffractometer PILATUS@ SNBL. *J. Synchrotron Radiat.* **2016**, *23*, 825−829.

(22) Coelho, A. A. TOPAS and TOPAS-Academic: an optimization program integrating computer algebra and crystallographic objects written in C++. *J. Appl. Crystallogr.* **2018**, *51*, 210−218.
(23) Perdew, J. P.; Burke, K.; Ernzerhof, M. Generalized gradient approximation made simple. *Phys. Rev. Lett.* **1996**, *77*, 3865.
(24) Giannozzi, P.; Baroni, S.; Bonini, N.; Calandra, M.; Car, R.; Cavazzoni, C.; Ceresoli, D.; Chiarotti, G. L.; Cococcioni, M.; Dabo, I.; Dal Corso, A.; de Gironcoli, S.; Fabris, S.; Fratesi, G.; Gebauer, R.; Gerstmann, U.; Gougoussis, C.; Kokalj, A.; Lazzeri, M.; Martin-Samos, L.; Marzari, N.; Mauri, F.; Mazzarello, R.; Paolini, S.; Pasquarello, A.; Paulatto, L.; Sbraccia, C.; Scandolo, S.; Sclauzero, G.; Seitsonen, A. P.; Smogunov, A.; Umari, P.; Wentzcovitch, R. M. QUANTUM ESPRESSO: a modular and open-source software project for quantum simulations of materials. *J. Phys.: Condens. Matter* **2009**, *21*, 395502.
(25) Vanderbilt, D. Soft self-consistent pseudopotentials in a generalized eigenvalue formalism. *Phys. Rev. B: Condens. Matter Mater. Phys.* **1990**, *41*, 7892.
(26) Garrity, K. F.; Bennett, J. W.; Rabe, K. M.; Vanderbilt, D. Pseudopotentials for high-throughput DFT calculations. *Comput. Mater.* **2014**, *81*, 446−452.
(27) Dal Corso, A. Pseudopotentials periodic table: From H to Pu. *Comput. Mater.* **2014**, *95*, 337−350.
(28) Poloni, R.; Lee, K.; Berger, R. F.; Smit, B.; Neaton, J. B. Understanding trends in CO2 adsorption in metal−organic frameworks with open-metal sites. *J. Phys. Chem. Lett.* **2014**, *5*, 861−865.
(29) Grimme, S. Semiempirical GGA-type density functional constructed with a long-range dispersion correction. *J. Comput. Chem.* **2006**, *27*, 1787−1799.
(30) Tkatchenko, A.; Scheffler, M. Accurate molecular van der Waals interactions from ground-state electron density and free-atom reference data. *Phys. Rev. Lett.* **2009**, *102*, 073005.
(31) Dincă, M.; Han, W. S.; Liu, Y.; Dailly, A.; Brown, C. M.; Long, J. R. Observation of Cu2+−H2 Interactions in a Fully Desolvated Sodalite-Type Metal−Organic Framework. *Angew. Chem. Int. Ed.* **2007**, *46*, 1419−1422.
(32) Li, X.-H.; Xia, F.-Y.; Xiao, H.-P.; Hu, M.-L. Hexaaquacopper (II) diperchlorate dihydrate. *Acta Crystallogr., Sect. E: Struct. Rep. Online* **2004**, *60*, i31−i32.
(33) Rulíšek, L.; Vondrášek, J. Coordination geometries of selected transition metal ions (Co2+, Ni2+, Cu2+, Zn2+, Cd2+, and Hg2+) in metalloproteins. *J. Inorg. Biochem.* **1998**, *71*, 115−127.
(34) Morosin, B. The crystal structures of copper tetrammine complexes. A. Cu (NH3) 4SO2. H2O and Cu (NH3) 4SeO4. *Acta Crystallogr., Sect. B: Struct. Crystallogr. Cryst. Chem.* **1969**, *25*, 19−30.
(35) Catalan, J.; Elguero, J. Basicity and acidity of azoles. *Adv. Heterocycl. Chem.* **1987**, *41*, 187−274.
(36) Greenwood, N. N.; Earnshaw, A. *Chemistry of the Elements*; Elsevier: Oxford, 2012.
(37) Queen, W. L.; Hudson, M. R.; Bloch, E. D.; Mason, J. A.; Gonzalez, M. I.; Lee, J. S.; Gygi, D.; Howe, J. D.; Lee, K.; Darwish, T. A.; James, M.; Peterson, V. K.; Teat, S. J.; Smit, B.; Neaton, J. B.; Long, J. R.; Brown, C. M. Comprehensive study of carbon dioxide adsorption in the metal−organic frameworks M 2 (dobdc)(M= Mg, Mn, Fe, Co, Ni, Cu, Zn). *Chem. Sci.* **2014**, *5*, 4569−4581.
(38) Wu, H.; Simmons, J. M.; Srinivas, G.; Zhou, W.; Yildirim, T. Adsorption Sites and Binding Nature of CO2 in Prototypical Metal−Organic Frameworks: A Combined Neutron Diffraction and First-Principles Study. *J. Phys. Chem. Lett.* **2010**, *1*, 1946−1951.
(39) Lu, Z.; Godfrey, H. G.; Da Silva, I.; Cheng, Y.; Savage, M.; Tuna, F.; McInnes, E. J.; Teat, S. J.; Gagnon, K. J.; Frogley, M. D. Modulating supramolecular binding of carbon dioxide in a redox-active porous metal-organic framework. *Nat. Commun.* **2017**, *8*, 14212.
(40) Giacobbe, C.; Lavigna, E.; Maspero, A.; Galli, S. Elucidating the CO 2 adsorption mechanisms in the triangular channels of the bis (pyrazolate) MOF Fe 2 (BPEB) 3 by in situ synchrotron X-ray diffraction and molecular dynamics simulations. *J. Mater. Chem. A* **2017**, *5*, 16964−16975.
(41) Yang, S.; Sun, J.; Ramirez-Cuesta, A. J.; Callear, S. K.; David, W. I. F.; Anderson, D. P.; Newby, R.; Blake, A. J.; Parker, J. E.; Tang, C. C.; Schröder, M. Selectivity and direct visualization of carbon dioxide and sulfur dioxide in a decorated porous host. *Nat. Chem.* **2012**, *4*, 887.
(42) Dubbeldam, D.; Walton, K. S.; Ellis, D. E.; Snurr, R. Q. Exceptional negative thermal expansion in isoreticular metal−organic frameworks. *Angew. Chem.* **2007**, *119*, 4580−4583.
(43) Han, S. S.; Goddard, W. A. Metal− Organic Frameworks Provide Large Negative Thermal Expansion Behavior. *J. Phys. Chem. C* **2007**, *111*, 15185−15191.
(44) Wu, Y.; Kobayashi, A.; Halder, G. J.; Peterson, V. K.; Chapman, K. W.; Lock, N.; Southon, P. D.; Kepert, C. J. Negative Thermal Expansion in the Metal−Organic Framework Material Cu3 (1, 3, 5-benzenetricarboxylate) 2. *Angew. Chem. Int. Ed.* **2008**, *47*, 8929−8932.
(45) Queen, W. L.; Brown, C. M.; Britt, D. K.; Zajdel, P.; Hudson, M. R.; Yaghi, O. M. Site-specific CO2 adsorption and zero thermal expansion in an anisotropic pore network. *J. Phys. Chem. C* **2011**, *115*, 24915−24919.
(46) Fogler, H. S. *Elements of Chemical Reaction Engineering*, 4th ed.; Prentice Hall PTR: Upper Saddle River, 2006.
(47) Tadashi, M. *Thermodynamics*; InTechOpen: Rijeka, 2011.
(48) Mason, J. A.; Sumida, K.; Herm, Z. R.; Krishna, R.; Long, J. R. Evaluating Metal-Organic Frameworks for Post-Combustion Carbon Dioxide Capture via Temperature Swing Adsorption. *Energy Environ. Sci.* **2011**, *4*, 3030−3040.
(49) Krishna, R. The Maxwell-Stefan Description of Mixture Diffusion in Nanoporous Crystalline Materials. *Microporous Mesoporous Mater.* **2014**, *185*, 30−50.
(50) Krishna, R. Methodologies for Evaluation of Metal-Organic Frameworks in Separation Applications. *RSC Adv.* **2015**, *5*, 52269−52295.
(51) Myers, A. L.; Prausnitz, J. M. Thermodynamics of Mixed Gas Adsorption. *AIChE J.* **1965**, *11*, 121−127.
(52) Krishna, R. Screening Metal-Organic Frameworks for Mixture Separations in Fixed-Bed Adsorbers using a Combined Selectivity/Capacity Metric. *RSC Adv.* **2017**, *7*, 35724−35737.
(53) Krishna, R. Methodologies for Screening and Selection of Crystalline Microporous Materials in Mixture Separations. *Sep. Purif. Technol.* **2018**, *194*, 281−300.

https://dx.doi.org/10.1021/acs.chemmater.9b04631
Chem. Mater. 2020, 32, 1526−1536

Supporting Information for:

Understanding how ligand functionalization influences CO_2 and N_2 adsorption in a sodalite metal-organic framework

*Mehrdad Asgari, Rocio Semino, Pascal A. Schouwink, Ilia Kochetygov, Jacob Tarver, Olga Trukhina, Rajamani Krishna, Craig M. Brown, Michele Ceriotti, and Wendy L. Queen**

XRD pattern of Cu-BTTri sample

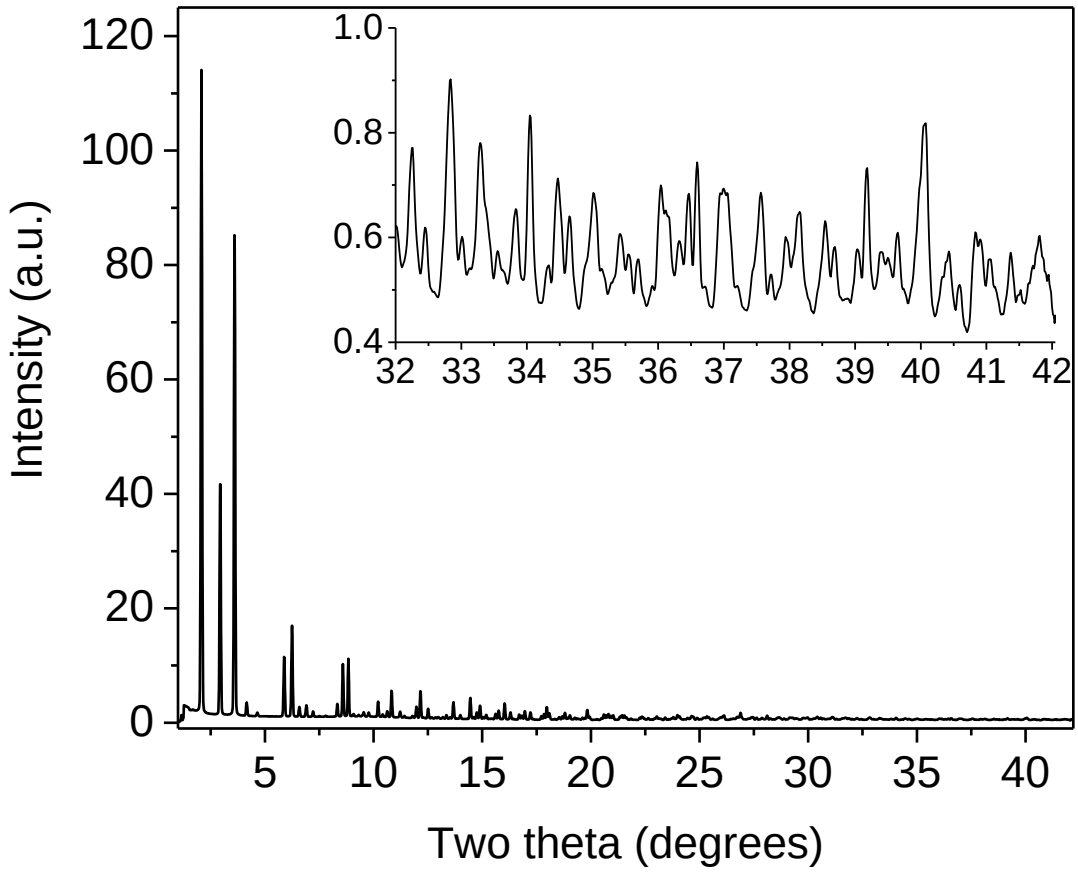

Figure S1. Synchrotron x-ray diffraction pattern collected on the bare Cu-BTTri in SNBL (BM01), ESRF. The wavelength is set to 0.67522 Å. The data confirms high crystallinity of the sample needed for the Rietveld analysis.

Gas adsorption measurements

UHP-grade (99.999 % purity) helium, nitrogen, and hydrogen were used for all adsorption measurements. Gas adsorption isotherms for pressures in the range 0–1 bar were measured using a BELSORP-max instrument. For standard measurements in BELSORP-max, the sample was transferred to pre-weighed low pressure resistant analysis tubes, which were capped with a Transeal. The sample was evacuated and heated on the activation stages of BELSORP-max based on the desired activation program. After finishing the activation program, the evacuated analysis tubes containing degassed sample was then carefully transferred to an electronic balance and weighed to determine the mass of sample (typically 100–200 mg). Then the tube was transferred to the analysis port of the gas adsorption instrument. Adsorption isotherms between 5 and 45°C were measured using a recirculating dewar (Micromeritics) connected to a Julabo F32-MC isothermal bath. For cryogenic measurements, the dewar vessel is used where is capable of keeping cryogenic baths under isolation. BET surface areas and pore volumes were determined by measuring N_2 adsorption isotherms in a 77 K liquid N_2 bath and calculated, assuming a value of 16.2 $Å^2$ for the molecular cross-sectional area of N_2.

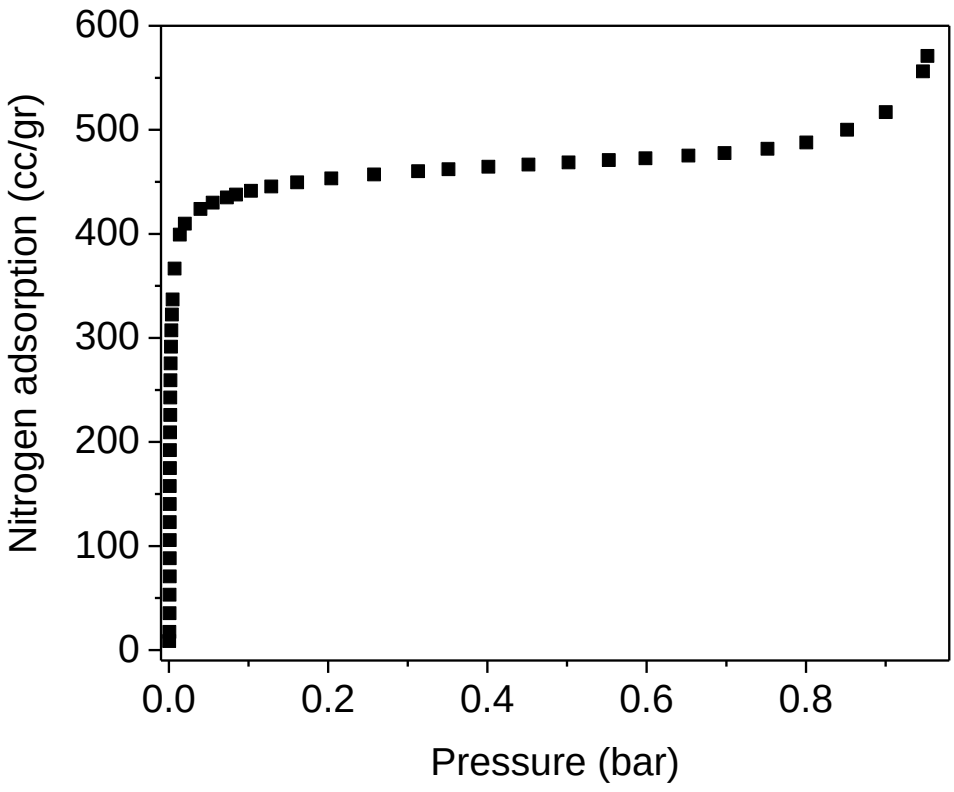

Figure S2. Nitrogen adsorption isotherm for Cu-BTTri collected at 77 K.

Pore Volume calculations based on the adsorption data for nitrogen at 77 K

As shown in Figure S2, the adsorption isotherm for N_2 at 77 K ceases to be a function of pressure when the pressure exceeds 200 mbar, implying that the structure has been saturated with nitrogen. Therefore, the uptake of N_2 at highest measured pressure can be considered as the full capacity of the framework for an inert small molecule, and the pore volume can then be calculated from the following formula:

$$Pore\ Volume = \frac{N_{N_2}^{Sat} * M_{w_{N_2}}}{1000 * d_{liqN_2}\big|_{77K}}$$

Where $N_{N_2}^{Sat}$ is the the amount of nitrogen adsorbed at the highest pressure point in mmol/g, $M_{w_{N_2}}$ is the molecular weight dinitrogen in g/mol and $d_{liqN_2}\big|_{77K}$ is the density of liquid nitrogen at 77 K in g/mL.

Surface area calculations based on the N_2 adsorption data at 77 K

Based on the BET theory, we have the following equation:

$$\frac{1}{N[\left(\frac{p_0}{p}\right) - 1]} = \frac{c-1}{N_m c}\left(\frac{p}{p_0}\right) + \frac{1}{N_m c}$$

Where N is the amount of gas adsorbed in mmol/g, N_m is the monolayer adsorption in mmol/g, p is the partial pressure of N_2 and p_0 is the saturation pressure of N_2 at the measurement temperature.[1] A plot of $\frac{1}{N[\left(\frac{p_0}{p}\right)-1]}$ versus $\frac{p}{p_0}$ and the best possible trendline is fit to the points on the plot. We note that points with low $\left(\frac{p}{p_0}\right)$ are chosen such that the *c* parameter stays positive and high R^2 values are obtained. With M as the slope and I as the intersect of the plot, N_m can be obtained from the following formula:

$$N_m = \frac{1}{M + I}$$

Thr surface area can then be obtained using the equation $SA = N_m \cdot N_A \cdot CSA_{N_2}$, where N_A is Avogadro's number and CSA_{N_2} is the cross sectional area of one N_2 molecule at 77 K (taken to be 16 $Å^2$). The above calculations were carried out on the nitrogen adsorption isotherm data collected at 77 K for Cu-BTTri; the resulting surface area has been reported in the paper.

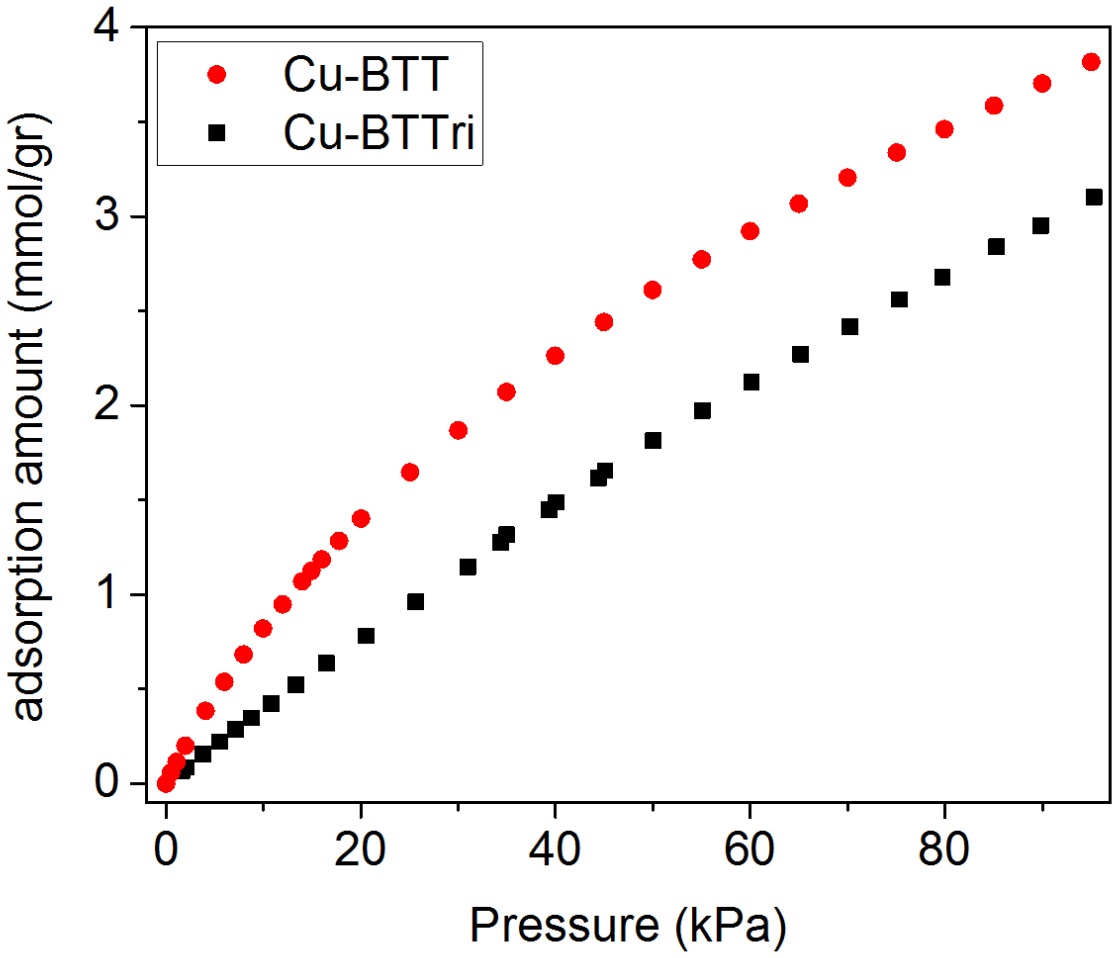

Figure S3. The comparison of carbon dioxide adsorption data for Cu-BTT and Cu-BTTri at 298K. The data for the adsorption data for Cu-BTT has been extracted from literature.[2]

Fitting Cu-BTTri CO_2 and N_2 adsorption isotherms

The CO_2 and N_2 adsorption isotherms collected at three different temperatures of 278 K, 288 K and 298 K were fitted with a dual-site Langmuir model (Eq. S1):

$$n = \frac{a\mathrm{b}P}{1+\mathrm{b}P} + \frac{\mathrm{cd}P}{1+\mathrm{d}P} \qquad \text{(S1)}$$

where n is the amount of CO_2 or N_2 adsorbed in mol/g, a and b are Langmuir parameter for the first adsorption site, c and d are Langmuir parameter for the second adsorption site and P is the pressure in Pa. The fitted parameters for each adsorption isotherm can be found in Tables S1 and S2 for CO_2 and N_2, respectively. The comparison of the experimental CO_2 and N_2 adsorption isotherms with the fitted dual-site Langmuir model based on the experimental data are shown in Fig. S4 and Fig. S5, respectively. The n and P have been rescaled to mmol/gr and bar in these figures, which are more common units for showing adsorption isotherms. The dual-site Langmuir model was chosen because of the validity of the theory behind this model for prediction of the interaction of heterogeneous surfaces with gas-phase small molecules. The use of a dual-site Langmuir model for fitting gas adsorption isotherm data and the extraction of isosteric heats of adsorption has been reported elsewhere.[3-5]

Calculating Isosteric heats of adsorption

The Clausius-Clapeyron equation (Eqn. S2) was used to calculate the isosteric heats of adsorption, $-Q_{st}$, for CO_2 and N_2 adsorption on Cu-BTTri, using the dual-site Langmuir-Freundlich fits at 278 K, 288 K, and 298 K.

$$(\ln P)_n = -\frac{Q_{st}}{R}\left(\frac{1}{T}\right) + C \qquad \text{(S2)}$$

Where, P is the pressure in any desired unit, n is the amount adsorbed mol/g, T is the temperature in K, R is the universal gas constant kJ/mol·K, and C is a constant. The isosteric heat of adsorption, $-Q_{st}$, was obtained from the slope of plots of $(\ln P)_n$ as a function of inverse T. The isosteric heats of adsorption for CO_2 and N_2 as a function of loading of the adsorbate in Cu-BTTri can be found in Figure S7 and S9.

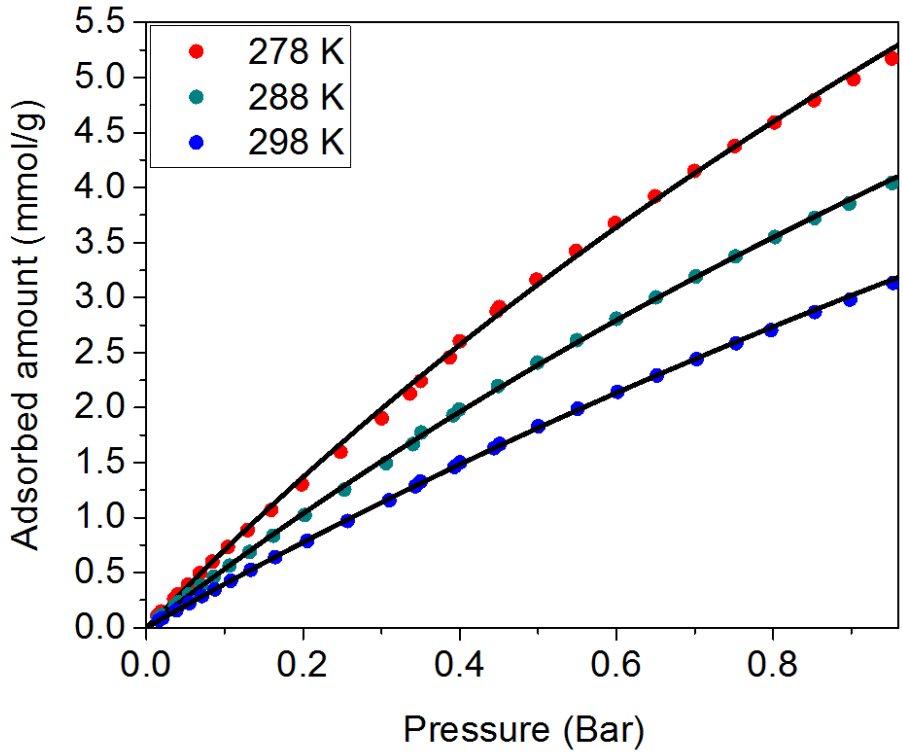

Figure S4. Dual-site Langmuir fits for CO_2 adsorption in Cu-BTTri at 278 K, 288 K, and 298 K.

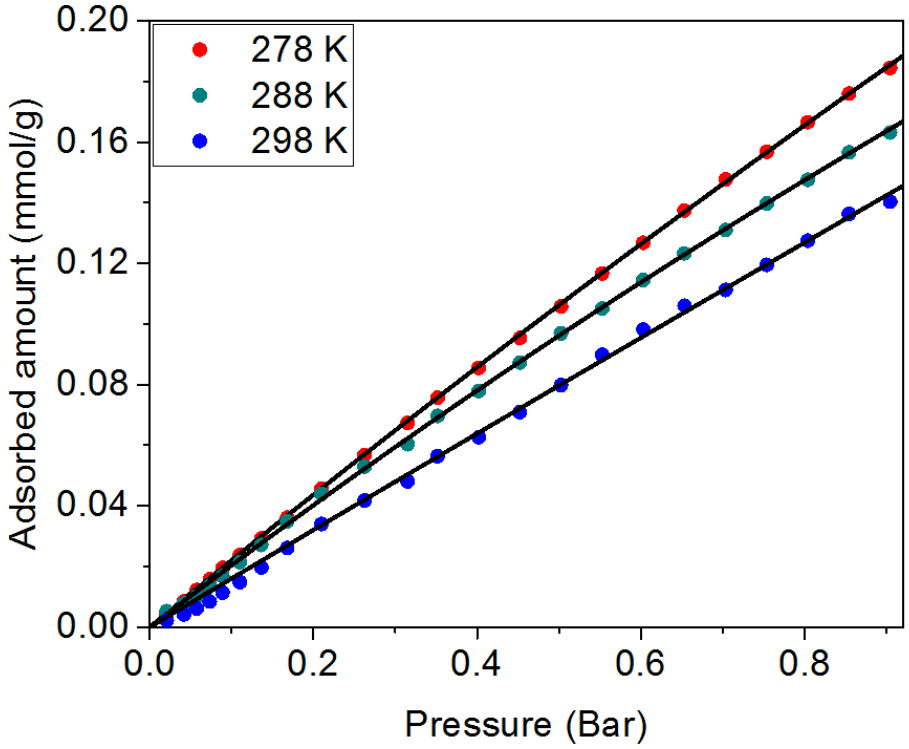

Figure S5. Dual-site Langmuir fits for N_2 adsorption in Cu-BTTri at 278 K, 288 K, and 298 K.

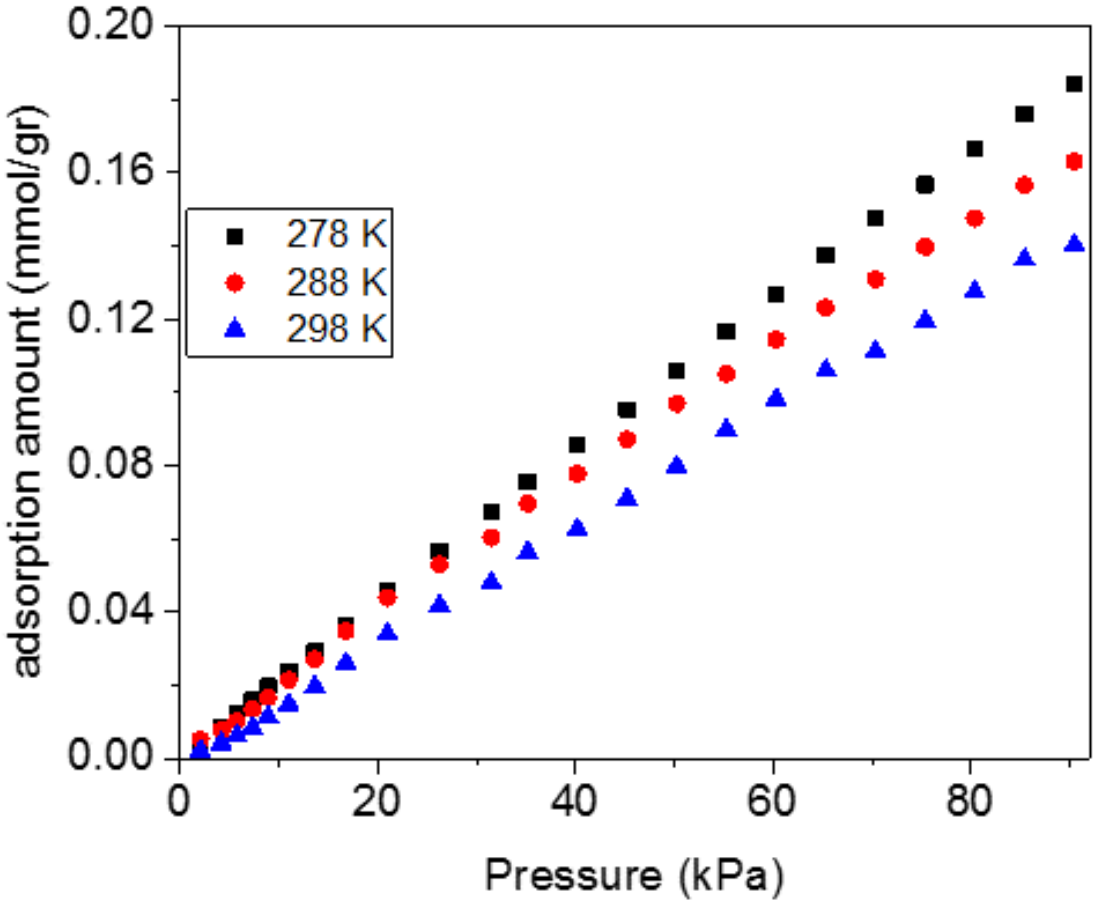

Figure S6. The measured N_2 adsorption isotherms for Cu-BTTri at different temperatures.

Table S1- Dual-site Langmuir parameters for CO_2 adsorption in Cu-BTTri at 278 K, 288 K, and 298 K.

	a	*b*	*c*	*d*
278 K	0.016748	3.927E-06	0.187684	3.967E-08
288 K	0.014541	3.415E-06	0.157244	3.406E-08
298 K	0.012518	2.800E-06	0.166689	3.343E-08

Table S2- Dual-site Langmuir parameters for N_2 adsorption in Cu-BTTri at 278 K, 288 K, and 298 K.

	a	*b*	*c*	*d*
278 K	2.622E-07	5.849E-06	2.379786	9.346E-07
288 K	2.961E-07	1.453E-06	1.331992	1.556E-06
298 K	1.275E-07	1.847E-06	9.005747	1.786E-07

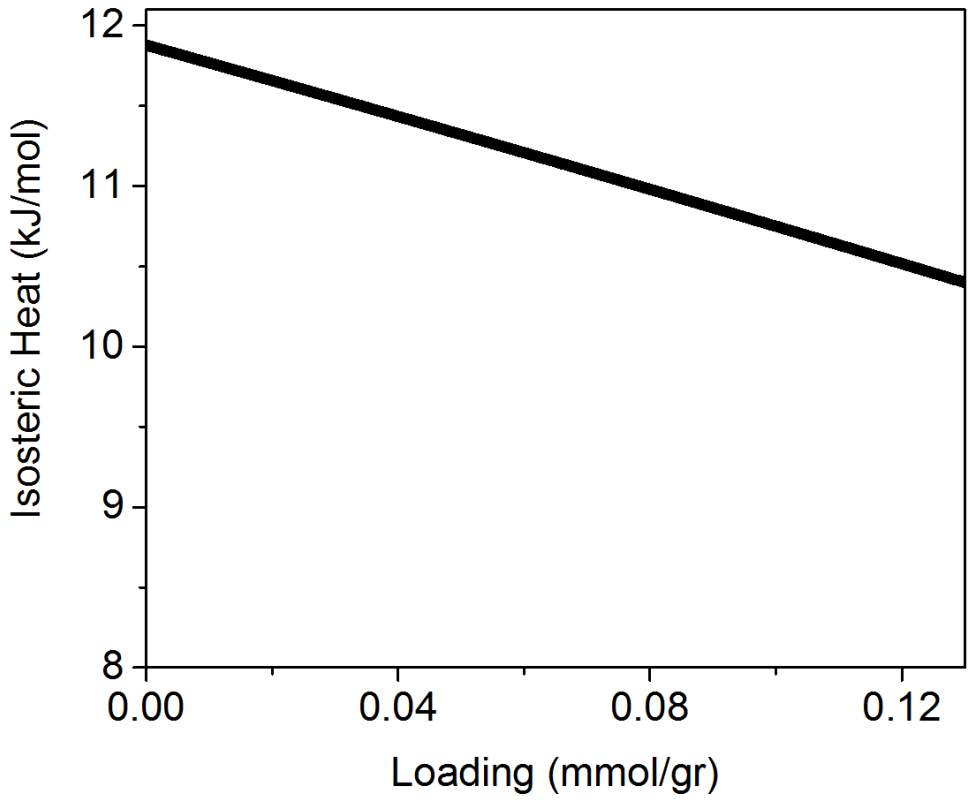

Figure S7. The N_2 isosteric heat of adsorption for Cu-BTTri obtained from Clasius-Clapeyron equation.

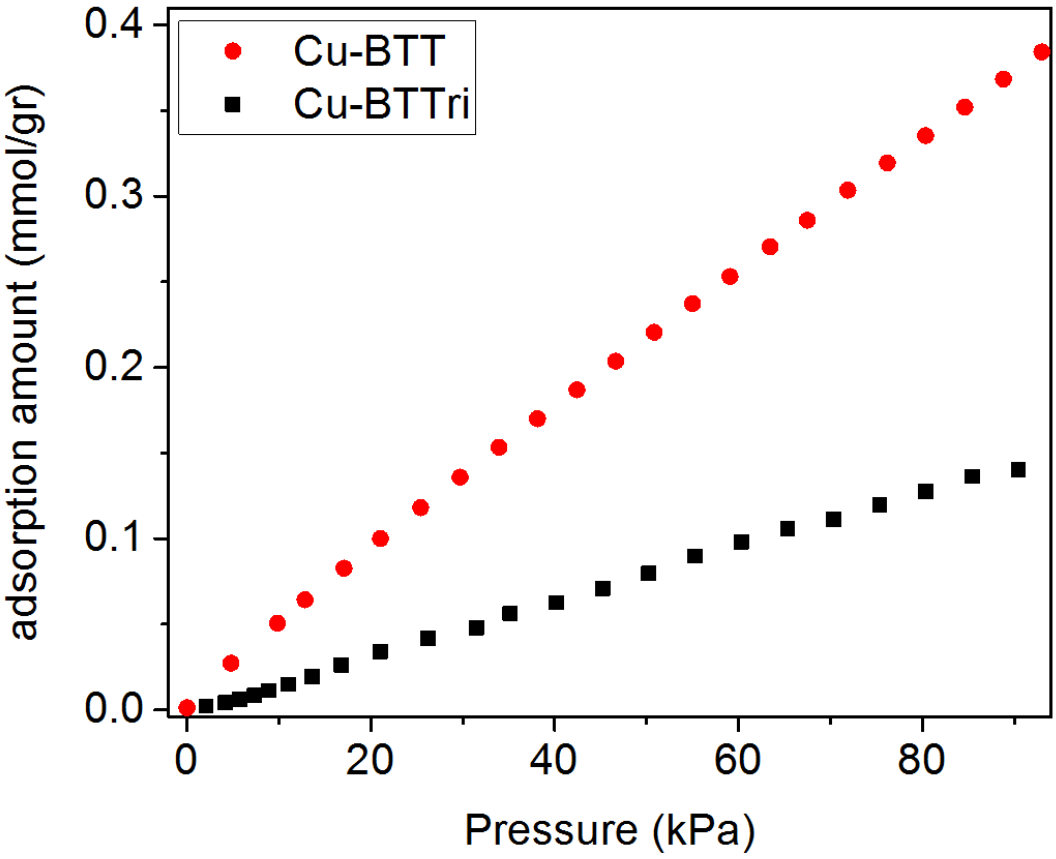

Figure S8. The comparison of nitrogen adsorption data for Cu-BTT and Cu-BTTri at 298K. The data for the adsorption data for Cu-BTT has been extracted from literature.[2]

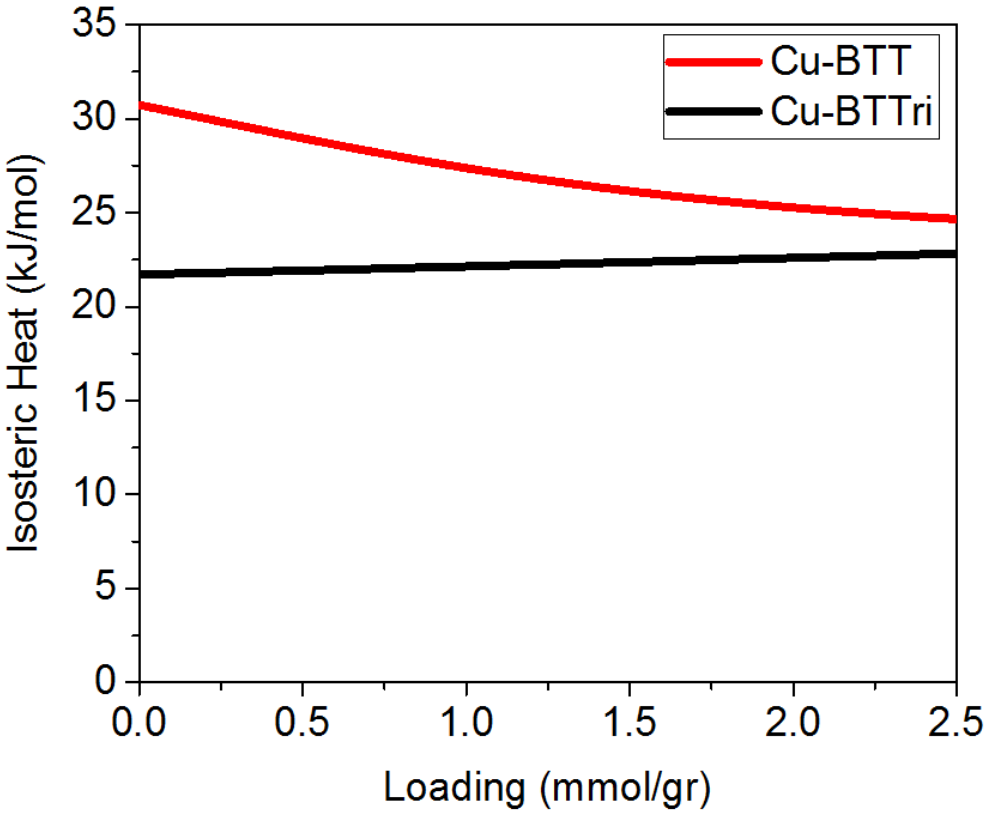

Figure S9. The comparison of CO_2 isosteric heat of adsorption for Cu-BTT and Cu-BTTri obtained by Clasius-Clapeyron equation. The data for the adsorption data for Cu-BTT has been extracted from literature.[2]

Table S3- Experimental and computed data for CO_2 adsorption sites in Cu-BTTri framework.

	Overall	**Site I**		**Site II**		**Site III**		**Site IV**	
	$-Q_{st}$ (kJ/mol)	$-H_b$ (kJ/mol)	Cu-O(CO_2)	$-H_b$ (kJ/mol)	N-O(CO_2)	$-H_b$ (kJ/mol)	C-O(CO_2)	$-H_b$ (kJ/mol)	O-N/C (triazole)
Experimental	21.7	-	2.86(7)	-	3.27(4)	-	2.8(1)	-	3.02(9) Å
DFT	-	25.0	2.96	26.5	3.16	17.0	3.42	15.8	≈ 3 Å

Table S4- Contributions to the binding energies for the four detected CO_2 adsorption sites in Cu-BTTri structure

Site No.	E_{PBE} (kJ/mol)	$E_{Dispersion\text{-}D2}$ (kJ/mol)
1	-7.412	-17.606
2	3.792	-30.259
3	-1.605	-15.390
4	0.054	-15.837

Isosurfaces of the charge density plots for CO_2 adsorption sites

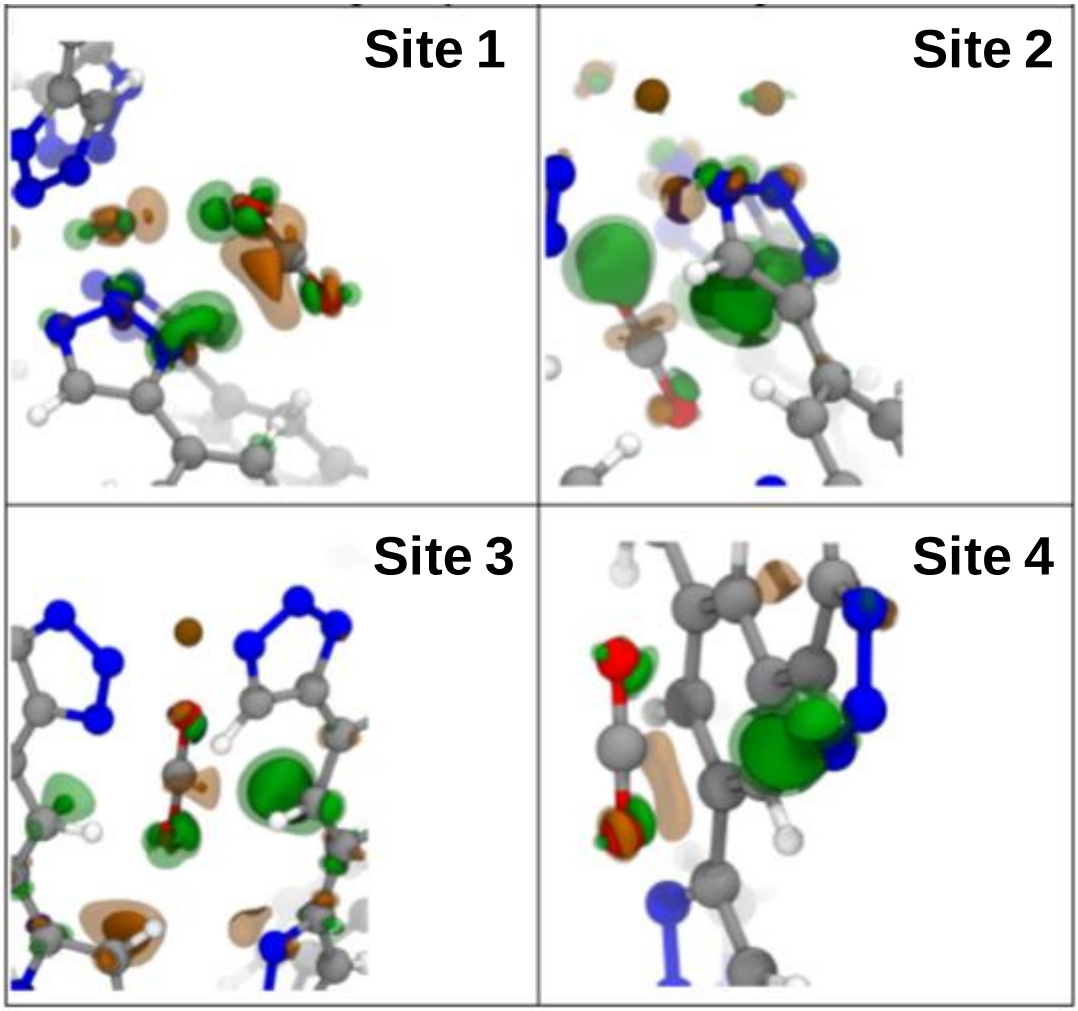

Figure S10. Schemes showing the four CO_2 adsorption sites and two isosurfaces of the charge density (negative=green, positive=orange) that are involved in the binding to Cu-BTTri.

Table S5- Contributions to the binding energies for the six detected N_2 adsorption sites in Cu-BTTri structure

Site No.	E_{PBE} (kJ/mol)	$E_{Dispersion-D2}$ (kJ/mol)	Total binding energy (kJ/mol)
1	-1.983	-9.927	-11.9
2	1.506	-18.544	-17.0
3	2.447	-14.074	-11.6
4	-0.631	-5.475	-6.1
5	1.926	-8.979	-7.1
6	0.167	-4.618	-4.5

Isosurfaces of the charge density plots for N_2 adsorption sites

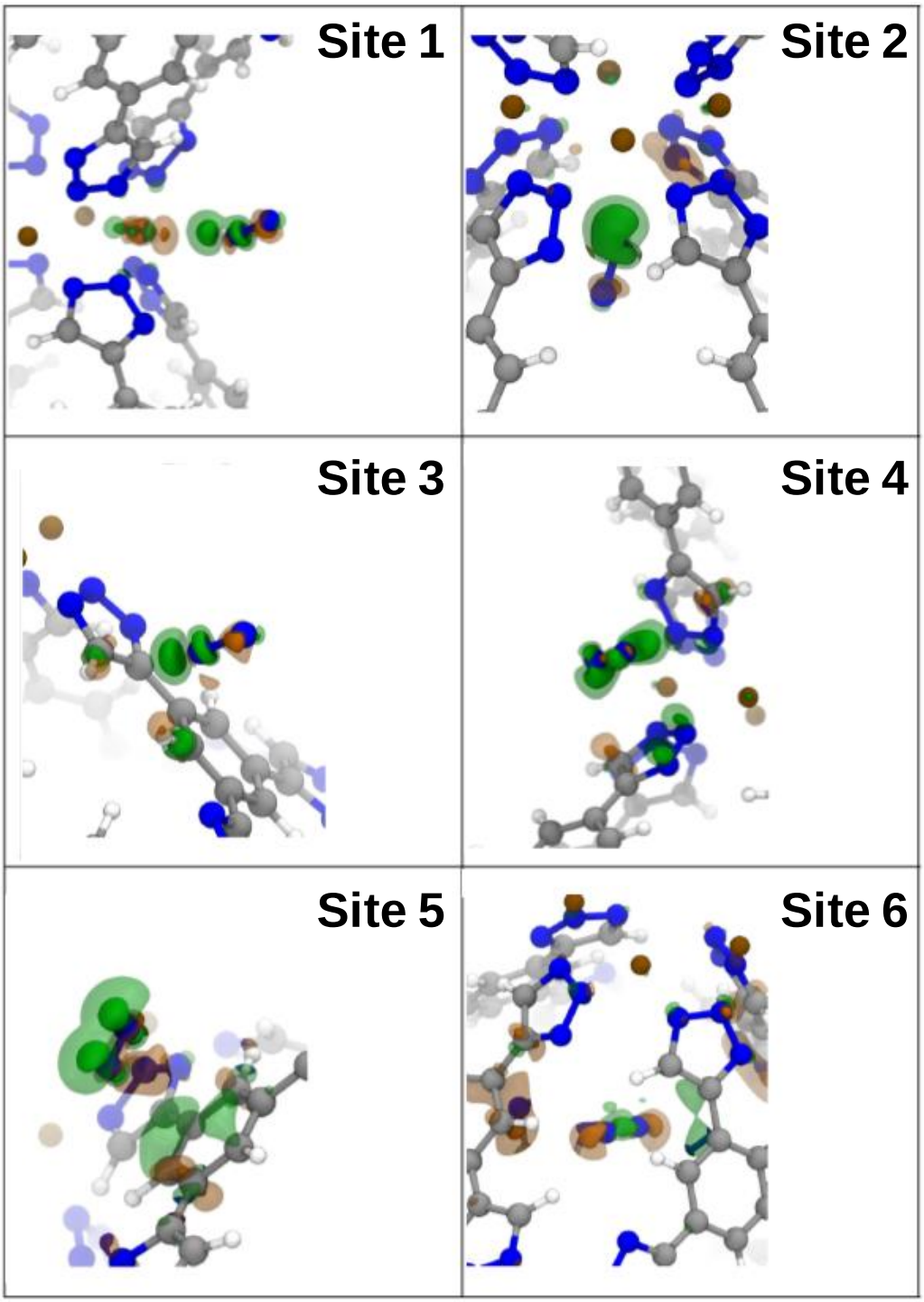

Figure S11. Schemes depicting the four N_2 adsorption sites and two isosurfaces of the charge density (negative=green, positive=orange) that are involved in the binding to CuBTTri.

Rietveld refinement of the framework loaded with 0.40 CO_2/Cu^{2+} (neutron diffraction data)

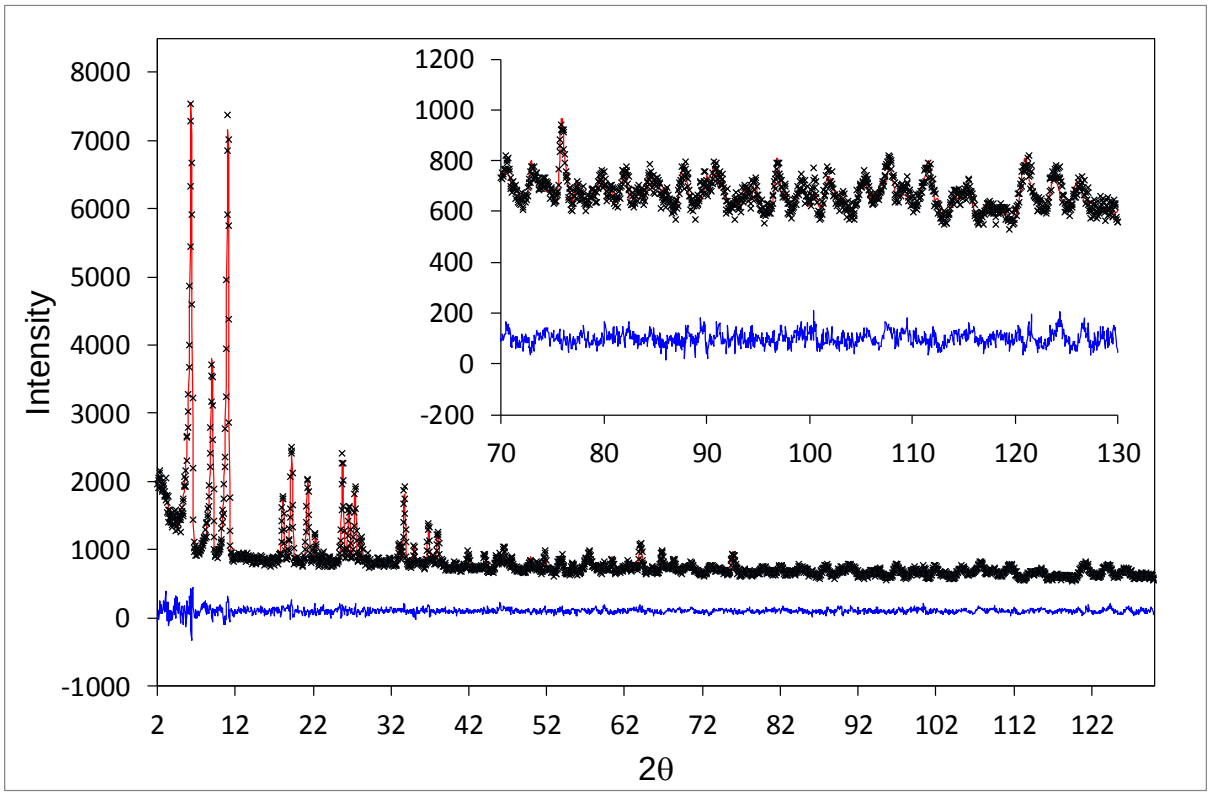

Figure S12. Neutron powder diffraction data collected at 10 K for a sample of Cu-BTTri loaded with 0.40 CO_2 per Cu site (38.4 CO_2 per unit cell). The green line, crosses, and red line represent the background, experimental, and calculated diffraction patterns, respectively. The blue line represents the difference between experimental and calculated patterns.

Table S6. Fractional atomic coordinates, occupancies, and isotropic displacement parameters obtained from Rietveld refinement of the structural model for Cu-BTTri loaded with 0.40 CO_2 per Cu site (38.4 CO_2 per unit cell) against diffraction data presented in Figure S12. The structure is cubic with Fm-3c space group, a = 37.070(2) Å, and V = 50942(7) $Å^3$. Values in parentheses represent standard deviation. GOF parameters: wRp = 0.0418, Rp = 0.0327. (The number for corresponding CIF file in CCDC database: 1893609).

Atom	x	y	z	occupancy	Biso ($Å^2$)
Cu1	0.5	0.3144(5)	0.7569(8)	1	1.0(6)
C1	0.3380(3)	0.6154(4)	0.3380(3)	1	1.9(3)
C3	0.3222(4)	0.6312(3)	0.3688(3)	1	1.9(3)
C2	0.3224(3)	0.5817(5)	0.3224(3)	1	1.9(3)
N1	0.2838(4)	0.5397(5)	0.3173(5)	1	1.9(2)
N2	0.3089(5)	0.5363(5)	0.2910(4)	1	1.9(2)
N3A	0.3336(6)	0.5624(6)	0.2933(7)	0.56038	1.9(2)
C1A	0.2924(8)	0.5672(7)	0.3389(7)	0.43962	1.9(2)
N3B	0.2924(8)	0.5672(7)	0.3389(7)	0.43962	1.9(2)
C1B	0.3336(6)	0.5624(6)	0.2933(7)	0.56038	1.9(2)
H1	0.301(1)	0.619(2)	0.380(2)	1	4.4(9)
H1A	0.282(4)	0.579(3)	0.362(4)	0.43962	4.4(9)
H1B	0.355(4)	0.570(3)	0.278(3)	0.56038	4.4(9)
O_new2a	0.391(3)	0.264(3)	0.75(1)	0.101(6)	6(8)
O_new2b	0.340(3)	0.299(3)	0.75(1)	0.101(6)	9(7)
C_new2c	0.366(3)	0.282(3)	0.75(1)	0.101(6)	9(7)
O_new1a	0.5	0.388(4)	0.760(4)	0.21(2)	8(6)
O_new1b	0.551(4)	0.418(8)	0.780(4)	0.106(9)	8(6)
C_new1c	0.525(2)	0.403(6)	0.770(4)	0.106(9)	8(6)

Rietveld refinement of the framework loaded with 1.25 CO_2/Cu^{2+} (neutron diffraction data)

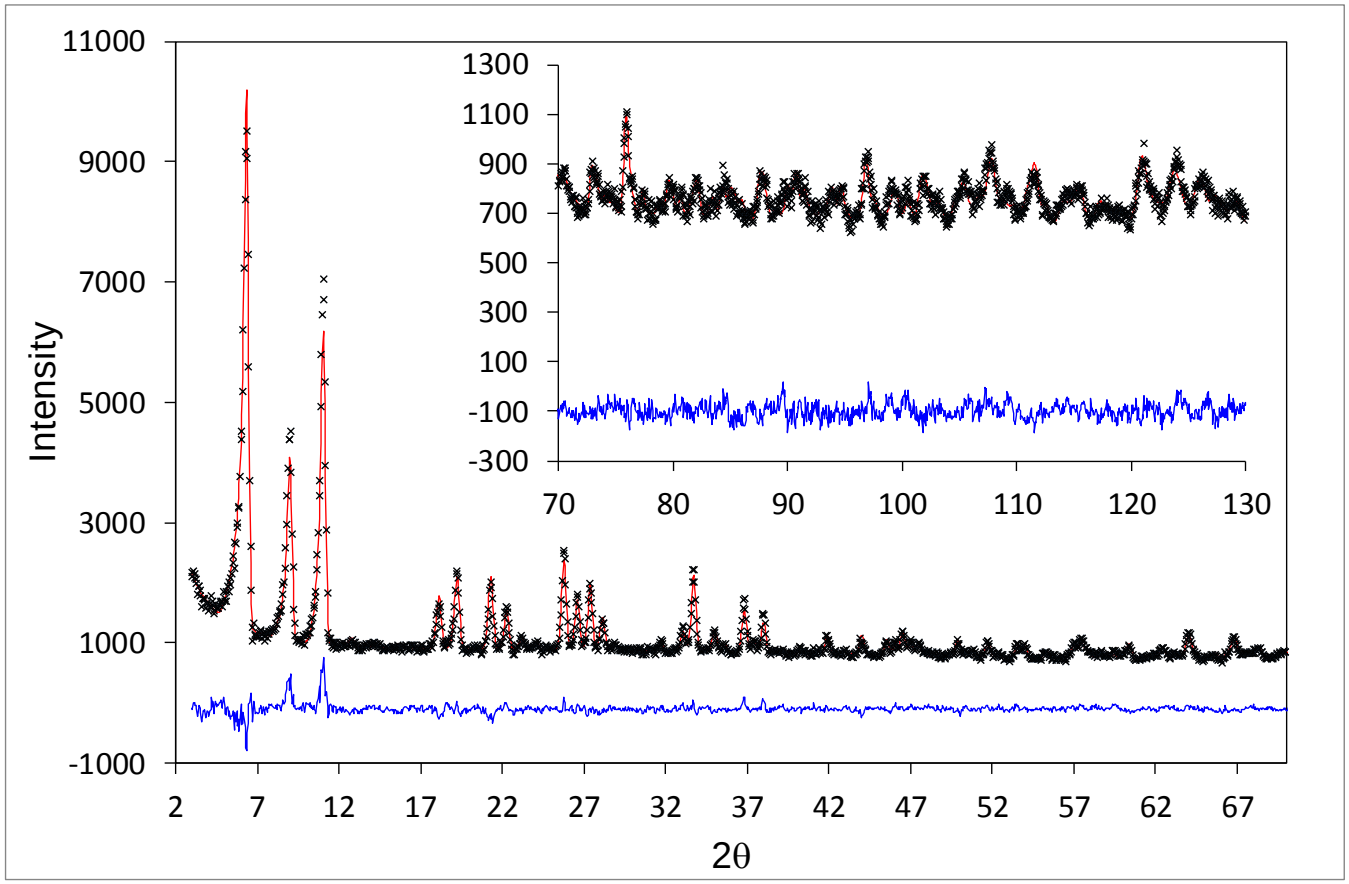

Figure S13. Neutron powder diffraction data collected at 10 K on a sample of Cu-BTTri loaded with 1.25 CO_2 per Cu site (120 CO_2 per unit cell). The green line, crosses, and red line represent the background, experimental, and calculated diffraction patterns, respectively. The blue line represents the difference between experimental and calculated patterns.

Table S7. Fractional atomic coordinates, occupancies, and isotropic displacement parameters obtained from Rietveld refinement of the structural model for Cu-BTTri loaded with 1.25 CO_2 per Cu site (120 CO_2 per unit cell) against diffraction data collected presented in Figure S13. The structure is cubic, space group Fm-3c, a = 37.072(2) Å, V = 50949(7) $Å^3$. Values in parentheses represent standard deviation. GOF parameters: wRp = 0.0474, Rp = 0.0369. (The number for corresponding CIF file in CCDC database: 1893608).

Atom	x	y	z	occupancy	Biso ($Å^2$)
Cu1	0.5	0.3153(5)	0.7566(10)	1	1.2(6)
C1	0.3374(3)	0.6152(4)	0.3374(3)	1	1.1(2)
C3	0.3222(4)	0.6300(3)	0.3700(3)	1	1.1(2)
C2	0.3225(3)	0.5817(5)	0.3225(3)	1	1.1(2)
N1	0.2850(5)	0.5381(6)	0.3159(6)	1	1.7(1)
N2	0.3093(5)	0.5372(6)	0.2913(5)	1	1.7(1)
N3A	0.3345(6)	0.5634(7)	0.2928(7)	0.56038	1.7(1)
C1A	0.2928(8)	0.5665(8)	0.3386(8)	0.43962	1.7(1)
N3B	0.2928(8)	0.5665(8)	0.3386(8)	0.43962	1.7(1)
C1B	0.3345(6)	0.5634(7)	0.2928(7)	0.56038	1.7(1)
H1	0.3017(9)	0.6156(14)	0.3789(13)	1	3.1(9)
H1A	0.279(4)	0.578(3)	0.361(4)	0.43962	3.1(9)
H1B	0.357(4)	0.572(3)	0.277(3)	0.56038	3.1(9)
O_new2a	0.411(2)	0.25	0.75	0.48(3)	2
O_new2b	0.360(2)	0.284(2)	0.750(8)	0.120(6)	0.37858
C_new2c	0.386(2)	0.267(2)	0.750(8)	0.120(6)	0.37858
O_new1a	0.5	0.394(2)	0.767(2)	0.739(19)	8.45671
O_new1b	0.559(3)	0.413(3)	0.780(3)	0.369(10)	8.45671
C_new1c	0.530(2)	0.403(3)	0.773(3)	0.369(10)	8.45671
C_new3a	0.228(2)	0.3134(9)	0.771(2)	0.128(5)	19.92848
O_new3b	0.246(2)	0.2950(9)	0.754(2)	0.128(5)	19.92848
O_new3c	0.210(2)	0.3318(9)	0.789(2)	0.128(5)	19.92848

Rietveld refinement of the framework loaded with 1.60 CO_2/Cu^{2+} (neutron diffraction data)

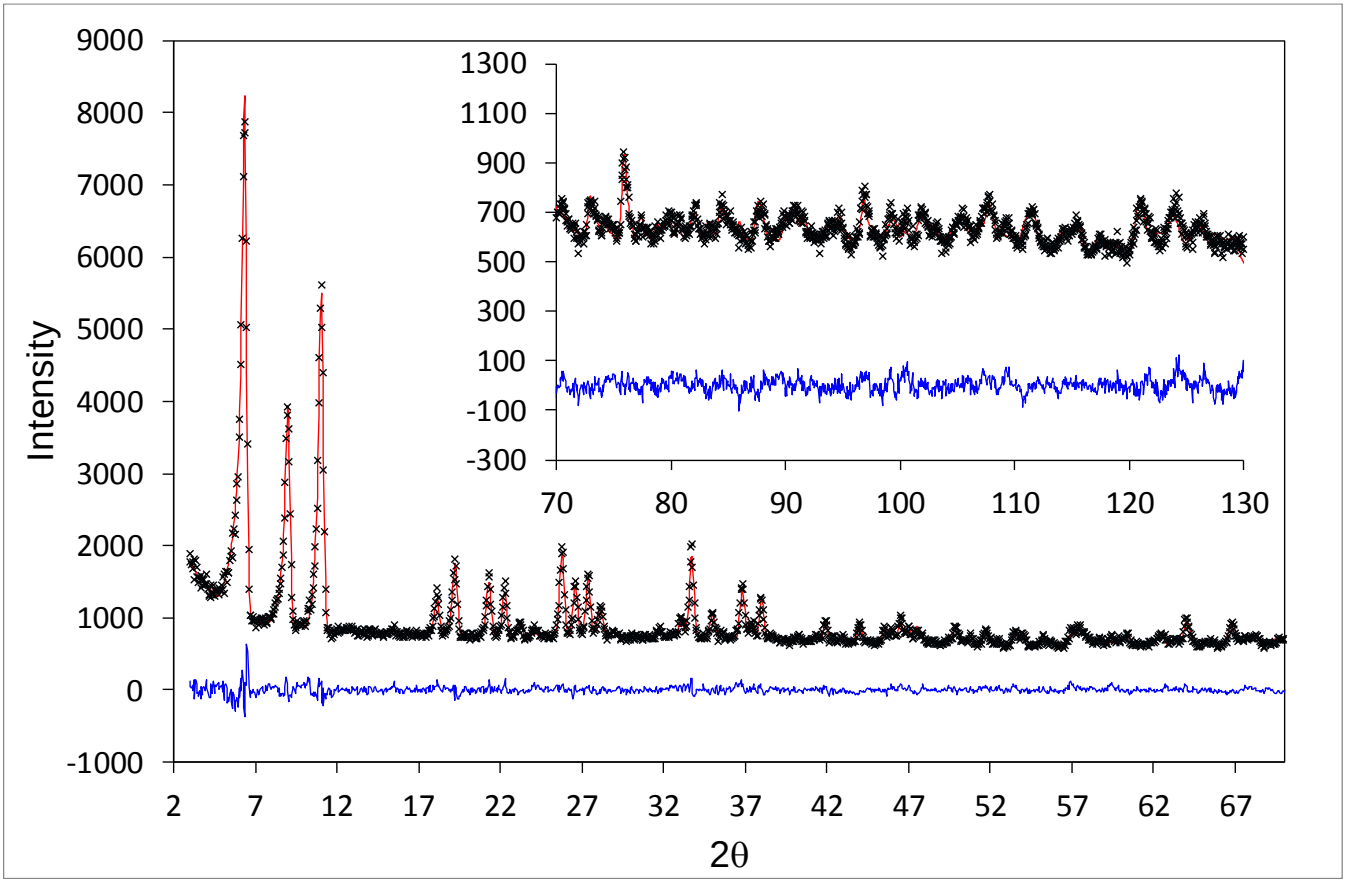

Figure S14. Neutron powder diffraction data collected at 10 K for a sample of Cu-BTTri loaded with 1.60 CO_2 per Cu site (153.6 CO_2 per unit cell). The green line, crosses, and red line represent the background, experimental, and calculated diffraction patterns, respectively. The blue line represents the difference between experimental and calculated patterns.

Table S8. Fractional atomic coordinates, occupancies, and isotropic displacement parameters obtained from Rietveld refinement of the structural model for Cu-BTTri loaded with 1.60 CO_2 per Cu site (153.6 CO_2 per unit cell) against diffraction data collected presented in Figure S14. The structure is cubic, space group Fm-3c, a = 37.070(1) Å, V = 50943(5) $Å^3$. Values in parentheses represent standard deviation. GOF parameters: wRp = 0.0460, Rp = 0.0362. (The number for corresponding CIF file in CCDC database: 1893610).

Atom	x	y	z	occupancy	Biso ($Å^2$)
Cu1	0.5	0.3156(5)	0.7566(8)	1	0.4(6)
C1	0.3366(3)	0.6162(4)	0.3366(3)	1	1.0(2)
C3	0.3224(4)	0.6306(3)	0.3694(3)	1	1.0(2)
C2	0.3218(3)	0.5823(5)	0.3218(3)	1	1.0(2)
N1	0.2848(5)	0.5385(5)	0.3175(5)	1	1.8(1)
N2	0.3077(5)	0.5363(5)	0.2915(4)	1	1.8(1)
N3A	0.3305(5)	0.5631(6)	0.2915(6)	0.56038	1.8(1)
C1A	0.2946(6)	0.5648(7)	0.3397(7)	0.43962	1.8(1)
N3B	0.2946(6)	0.5648(7)	0.3397(7)	0.43962	1.8(1)
C1B	0.3305(5)	0.5631(6)	0.2915(6)	0.56038	1.8(1)
H1	0.297(1)	0.625(2)	0.382(2)	1	6.0(1)
H1A	0.282(4)	0.577(4)	0.363(4)	0.43962	6.0(1)
H1B	0.349(4)	0.568(3)	0.272(3)	0.56038	6.0(1)
O_new2a	0.411(1)	0.25	0.75	0.67(3)	2
O_new2b	0.360(1)	0.284(2)	0.753(4)	0.168(8)	0.68754
C_new2c	0.386(2)	0.267(2)	0.752(4)	0.168(8)	0.68754
O_new1a	0.5	0.392(2)	0.766(2)	0.82(2)	5.4171
O_new1b	0.553(2)	0.418(2)	0.785(2)	0.411(9)	5.4171
C_new1c	0.527(2)	0.404(2)	0.775(2)	0.411(9)	5.4171
O_new4a	0.334(6)	0.983(6)	0.609(6)	0.09(2)	20
O_new4b	0.379(6)	0.983(6)	0.652(6)	0.09(2)	20
C_new4c	0.356(6)	0.983(6)	0.630(6)	0.09(2)	20
C_new3a	0.331(2)	0.313(2)	0.767(4)	0.124(8)	15.83856
O_new3b	0.348(2)	0.295(2)	0.749(4)	0.124(8)	15.83856
O_new3c	0.314(2)	0.332(2)	0.785(4)	0.124(8)	15.83856

Rietveld refinement of the framework loaded with 0.33 N_2/Cu^{2+} (neutron diffraction data)

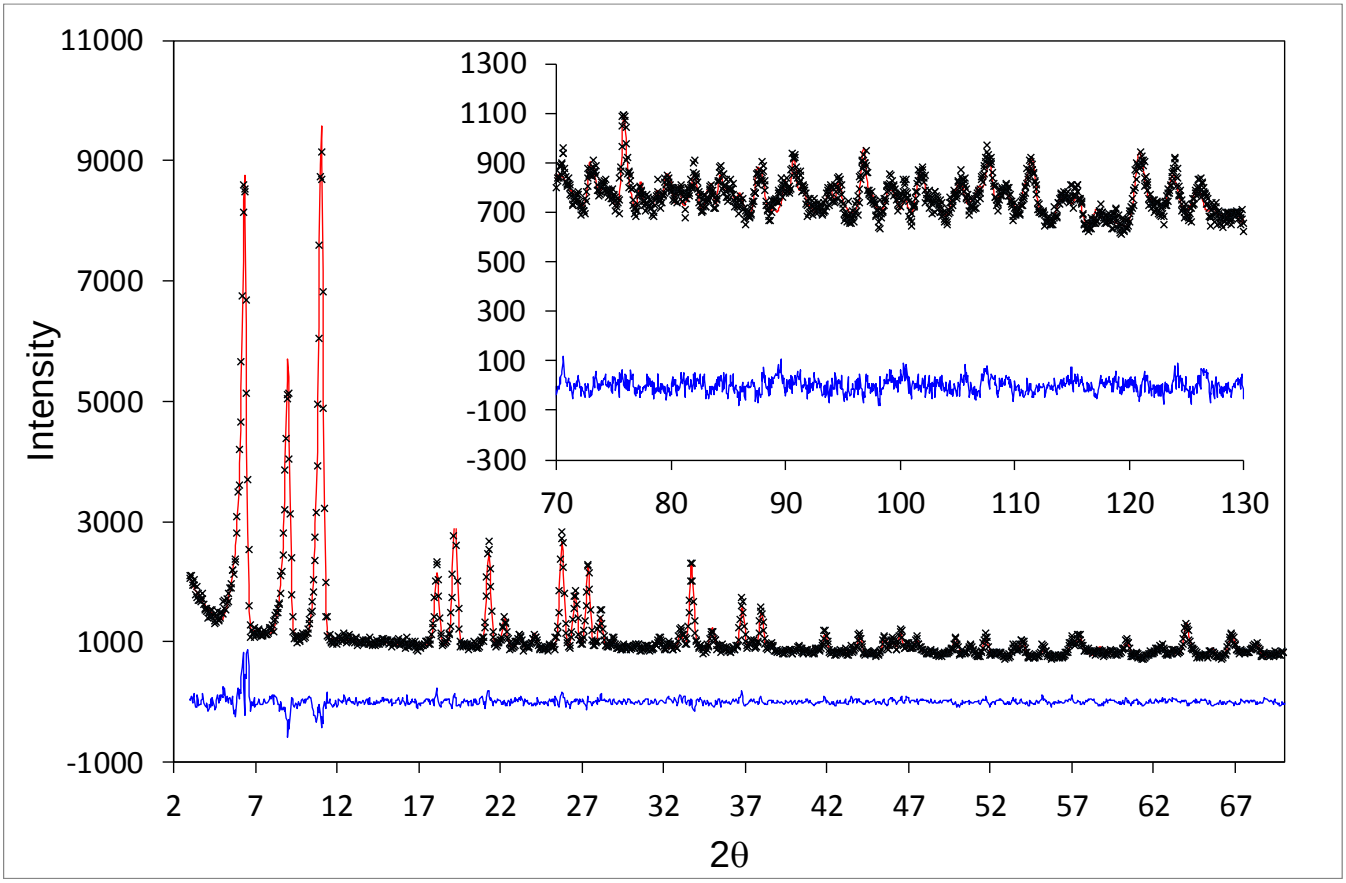

Figure S15. Neutron powder diffraction data collected at 10 K for a sample of Cu-BTTri loaded with 0.33 N_2 per Cu site (31.7 N_2 per unit cell). The green line, crosses, and red line represent the background, experimental, and calculated diffraction patterns, respectively. The blue line represents the difference between experimental and calculated patterns.

Table S9. Fractional atomic coordinates, occupancies, and isotropic displacement parameters obtained from Rietveld refinement of the structural model for Cu-BTTri loaded with 0.33 N_2 per Cu site (31.7 N_2 per unit cell) against diffraction data collected presented in Figure S15. The structure is cubic, space group Fm-3c, a = 37.078(1) Å, V = 50974(6) $Å^3$. Values in parentheses represent standard deviation. GOF parameters: wRp = 0.0407, Rp = 0.0348. (The number for corresponding CIF file in CCDC database: 1893610).

Atom	x	y	z	occupancy	Biso ($Å^2$)
Cu1	0.2446(6)	0.5	0.3158(5)	1	0.39406
C1	0.3370(2)	0.6162(3)	0.3370(2)	1	1.63372
C3	0.3219(3)	0.6312(2)	0.3688(2)	1	1.63372
C2	0.3220(2)	0.5831(4)	0.3220(2)	1	1.63372
N1	0.2838(4)	0.5389(4)	0.3161(4)	1	1.77941
N2	0.3090(4)	0.5344(4)	0.2913(3)	1	1.77941
N3A	0.3317(5)	0.5620(4)	0.2940(5)	0.56038	1.77941
C1A	0.2912(6)	0.5672(5)	0.3364(6)	0.43962	1.77941
N3B	0.2912(6)	0.5672(5)	0.3364(6)	0.43962	1.77941
C1B	0.3317(5)	0.5620(4)	0.2940(5)	0.56038	1.77941
H1	0.3015(9)	0.621(1)	0.383(1)	1	5.5799
H1A	0.276(4)	0.577(3)	0.359(3)	0.43962	5.5799
H1B	0.350(3)	0.570(3)	0.275(3)	0.56038	5.5799
N1_1	0.386(2)	0.509(3)	0.738(3)	0.145(7)	5.8349
N1_2	0.408(2)	0.512(3)	0.757(4)	0.145(7)	5.1375
N2_1	0.245(9)	0.605(6)	0.737(9)	0.020(4)	0.5
N2_2	0.229(9)	0.623(6)	0.755(9)	0.020(4)	0.5

Rietveld refinement of the framework loaded with 2.19 N_2/Cu^{2+} (neutron diffraction data)

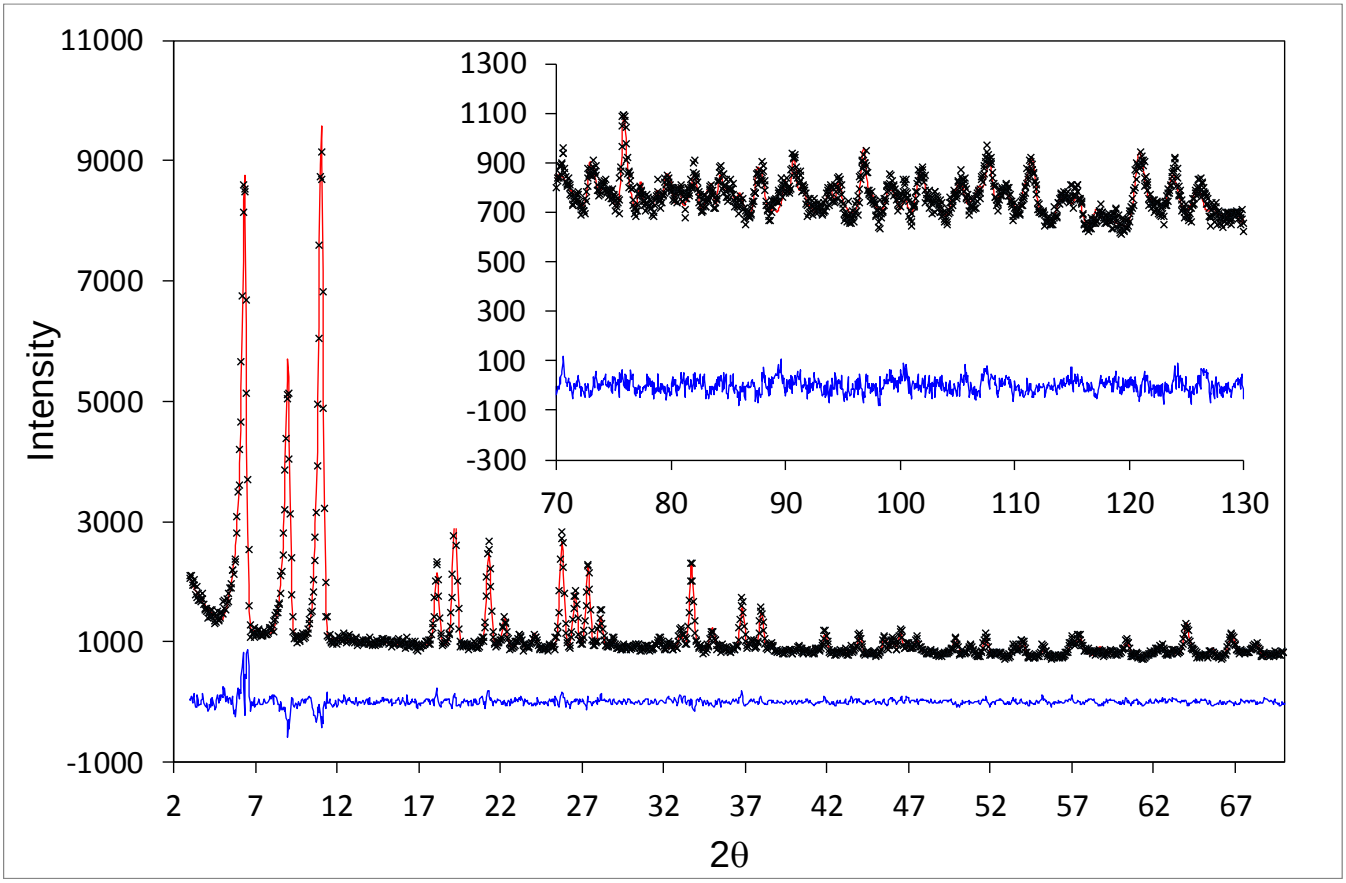

Figure S16. Neutron powder diffraction data collected at 10 K for a sample of Cu-BTTri loaded with 2.19 N_2 per Cu site (210 N_2 per unit cell). The green line, crosses, and red line represent the background, experimental, and calculated diffraction patterns, respectively. The blue line represents the difference between experimental and calculated patterns.

Table S10. Fractional atomic coordinates, occupancies, and isotropic displacement parameters obtained from Rietveld refinement of the structural model for Cu-BTTri loaded with 2.19 N_2 per Cu site (210 N_2 per unit cell) against diffraction data collected presented in Figure S16. The structure is cubic, space group Fm-3c, a = 37.098(2) Å, V = 51057(7) $Å^3$. Values in parentheses represent standard deviation. GOF parameters: wRp = 0.0420, Rp= 0.0356. (The number for corresponding CIF file in CCDC database: 1893606).

Atom	x	y	z	occupancy	Biso ($Å^2$)
Cu1	0.2457(8)	0.5	0.3153(5)	1	0.69447
C1	0.3370(3)	0.6165(4)	0.3370(3)	1	1.4(2)
C3	0.3228(4)	0.6310(3)	0.3690(3)	1	1.4(2)
C2	0.3218(3)	0.5819(5)	0.3218(3)	1	1.4(2)
N1	0.2839(4)	0.5394(5)	0.3159(5)	1	1.8(2)
N2	0.3092(5)	0.5345(4)	0.2917(4)	1	1.8(2)
N3A	0.3327(5)	0.5614(5)	0.2934(6)	0.56038	1.8(2)
C1A	0.2911(7)	0.5674(6)	0.3360(7)	0.43962	1.8(2)
N3B	0.2911(7)	0.5674(6)	0.3360(7)	0.43962	1.8(2)
C1B	0.3327(5)	0.5614(5)	0.2934(6)	0.56038	1.8(2)
H1	0.302(1)	0.621(1)	0.383(1)	1	4.6(9)
H1A	0.277(3)	0.577(3)	0.360(3)	0.43962	4.6(9)
H1B	0.350(3)	0.570(3)	0.275(3)	0.56038	4.6(9)
N1_1	0.389(1)	0.501(7)	0.7380(1)	0.296(9)	2.71822
N1_2	0.412(1)	0.509(3)	0.751(5)	0.296(9)	13.27875
N6_1	0.180(4)	0.75	0.765(5)	0.041(10)	0.5
N2_1	0.2665(7)	0.607(2)	0.741(2)	0.149(8)	20
N2_2	0.2504(7)	0.624(2)	0.758(2)	0.149(8)	20
N3_1	0.503(5)	0.362(2)	0.854(2)	0.29(1)	5
N3_2	0.508(2)	0.343(1)	0.875(2)	0.29(1)	5
N4_1	0.452(3)	0.453(3)	0.670(2)	0.28(1)	16.33157
N4_2	0.437(3)	0.437(3)	0.690(2)	0.28(1)	16.33157
N5_1	0.413(4)	0.405(5)	0.895(4)	0.057(6)	1
N5_2	0.390(4)	0.419(5)	0.909(4)	0.057(6)	1

Rietveld refinement of the framework loaded with 1.09 CO_2/Cu^{2+} (synchrotron diffraction data)

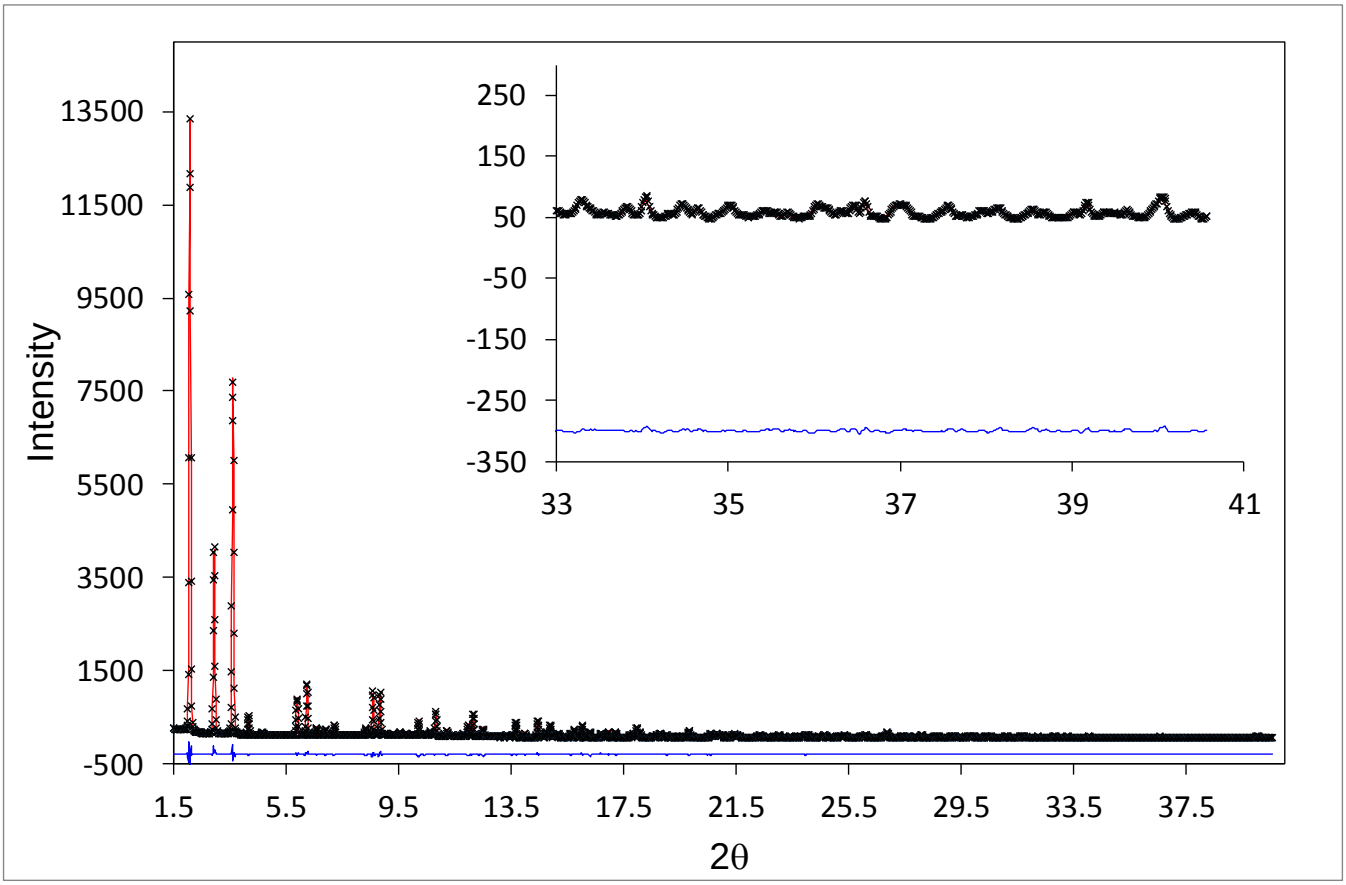

Figure S17. Synchrotron powder diffraction data collected at 100 K for a sample of Cu-BTTri loaded with 1.09 CO_2 per Cu site (104.6 CO_2 per unit cell). The green line, crosses, and red line represent the background, experimental, and calculated diffraction patterns, respectively. The blue line represents the difference between experimental and calculated patterns.

Table S11. Fractional atomic coordinates, occupancies, and isotropic displacement parameters obtained from Rietveld refinement of the structural model for Cu-BTTri loaded with 1.09 CO_2 per Cu site (104.6 CO_2 per unit cell) against diffraction data collected presented in Figure S17. The structure is cubic, space group Fm-3c, a = 37.091(9) Å, V = 51027(69) $Å^3$. Values in parentheses represent standard deviation. GOF parameters: wRp = 0.0409, Rp = 0.0285. (The number for corresponding CIF file in CCDC database: 1894884).

Atom	x	y	z	occupancy	Biso ($Å^2$)
Cu1	0.5	0.31340(6)	0.75456(7)	1	1
C1	0.3369(2)	0.6163(3)	0.3369(2)	1	1
C3	0.3223(2)	0.63127(18)	0.36873(18)	1	1
C2	0.3226(2)	0.5854(3)	0.3226(2)	1	2
N1	0.2832(3)	0.5407(3)	0.3177(3)	1	1
N2	0.3086(3)	0.5356(3)	0.2927(3)	1	1
N3A	0.3333(4)	0.5633(3)	0.2955(3)	0.56038	1
C1A	0.2901(4)	0.5714(4)	0.3375(4)	0.43962	1
N3B	0.2901(4)	0.5714(4)	0.3375(4)	0.43962	1
C1B	0.3333(4)	0.5633(3)	0.2955(3)	0.56038	1
O_new2a	0.4079(11)	0.25	0.75	0.66(3)	12
O_new2b	0.3565(11)	0.284(3)	0.749(9)	0.165(8)	20
C_new2c	0.3824(11)	0.267(3)	0.748(9)	0.165(8)	20
O_new1a	0.5	0.390(2)	0.762(2)	0.472(9)	18
O_new1b	0.559(2)	0.409(2)	0.774(2)	0.236(5)	18
C_new1c	0.529(3)	0.400(4)	0.768(5)	0.236(5)	18
O_new4a	0.326(6)	1.0(6)	0.608(6)	0.032(6)	12
O_new4b	0.371(6)	1.0(6)	0.652(6)	0.032(6)	12
C_new4c	0.348(6)	1.0(6)	0.630(6)	0.032(6)	12
C_new3a	0.326(6)	0.293(9)	0.770(13)	0.111(7)	20
O_new3b	0.348(5)	0.280(5)	0.753(11)	0.111(7)	20
O_new3c	0.303(9)	0.305(15)	0.787(15)	0.111(7)	20

Fitting of unary isotherm data for transient breakthrough simulations

The unary isotherm data for CO_2 and N_2 in CuBTT and CuBTTri were fitted with good accuracy using the single-site Langmuir model

$$q = q_{sat}\frac{bp}{1+bp} \quad (1)$$

The fitted parameter values are presented in Table S12 and Table S13.

Table S12. Single-site Langmuir parameter fits for CO_2 and N_2 in CuBTT at 298 K.

	q_{sat} mol kg^{-1}	b Pa^{-1}
CO_2	6.4	1.44E-05
N_2	6.4	6.93E-07

Table S13. Single-site Langmuir parameter fits for CO_2 and N_2 in CuBTTri at 298 K.

	q_{sat} mol kg^{-1}	b Pa^{-1}
CO_2	15	2.73E-06
N_2	15	9.81E-08

References

(1) Brunauer, S.; Emmett, P. H.; Teller, E. Adsorption of gases in multimolecular layers. *Journal of the American chemical society* **1938,** *60* (2), 309-319.
(2) Asgari, M.; Jawahery, S.; Bloch, E. D.; Hudson, M. R.; Flacau, R.; Vlaisavljevich, B.; Long, J. R.; Brown, C. M.; Queen, W. L. An experimental and computational study of CO 2 adsorption in the sodalite-type M-BTT (M= Cr, Mn, Fe, Cu) metal–organic frameworks featuring open metal sites. *Chemical science* **2018,** *9* (20), 4579-4588.
(3) Mason, J. A.; Sumida, K.; Herm, Z. R.; Krishna, R.; Long, J. R. Evaluating metal–organic frameworks for post-combustion carbon dioxide capture via temperature swing adsorption. *Energy & Environmental Science* **2011,** *4* (8), 3030-3040.
(4) Mathias, P. M.; Kumar, R.; Moyer, J. D.; Schork, J. M.; Srinivasan, S. R.; Auvil, S. R.; Talu, O. Correlation of multicomponent gas adsorption by the dual-site Langmuir model. Application to nitrogen/oxygen adsorption on 5A-zeolite. *Industrial & engineering chemistry research* **1996,** *35* (7), 2477-2483.
(5) McDonald, T. M.; D'Alessandro, D. M.; Krishna, R.; Long, J. R. Enhanced carbon dioxide capture upon incorporation of N, N′-dimethylethylenediamine in the metal–organic framework CuBTTri. *Chemical Science* **2011,** *2* (10), 2022-2028.